Muon $g-2$ in a type-X 2HDM assisted by inert scalars: A test at the ILC

Nabarun Chakrabarty[*] and Indrani Chakraborty[†,‡]

Department of Physics, Indian Institute of Technology Kanpur, Kanpur, Uttar Pradesh-208016, India

(Received 1 January 2023; accepted 16 February 2023; published 14 April 2023)

A two-Higgs doublet model can predict the observed muon $g-2$ for an appropriately light pseudoscalar that now faces tight constraints. However, it was shown recently in the companion paper [N. Chakrabarty, Muon $g-2$ in a type-X 2HDM assisted by inert scalars: A test at the LHC, preceding paper, arXiv:2112.13126.] that augmenting the two-Higgs doublet model by an additional inert doublet can lead to an explanation to the muon $g-2$ anomaly for a much heavier pseudoscalar. In this study, we probe such a framework at the proposed International Linear Collider using beam polarization for $\sqrt{s} = 1$ TeV. Using multivariate techniques, we analyze the signals $e^+e^- \to \tau^+\tau^- +$ missing transverse energy and $e^+e^- \to \mu^+\mu^- +$ missing transverse energy in the lepton- and muon-specific versions of the framework, respectively. Our analysis reveals that the e^+e^- machine operating at a 3000 fb^{-1} luminosity predicts a 5σ discovery of a pseudoscalar as heavy as 400 GeV. Comparing with the companion paper, it is concluded that the International Linear Collider is a much more potent machine than the LHC in this regard.

DOI: 10.1103/PhysRevD.107.075013

I. INTRODUCTION

A point of contention within the Standard Model (SM) is its failure to account for the observed value of the muon anomalous magnetic moment [1–12]. A combination of the results reported by BNL [13] and FNAL [14] shows that the discrepancy is

$$\Delta a_\mu \equiv a_\mu^{\rm exp} - a_\mu^{\rm SM} = 251(59) \times 10^{-11}. \tag{1}$$

A two-Higgs doublet model (2HDM) with flavor conserving Yukawa interactions of the type-X texture has long been known to address this anomaly [15–33]. And this happens for a high $\tan\beta$ ($\gtrsim$20) and a low pseudoscalar mass ($\lesssim$70 GeV). However, lepton universality constraints tend to rule out $\tan\beta \gtrsim 50$ [23]. Also, the Large Hadron Collider (LHC) search $h_{125} \to AA \to 4\tau, 2\tau 2\mu$ [34] stringently constrains the type-X 2HDM parameter region for $M_A < M_h/2 = 62.5$ GeV. In all, the model parameter space favoring the observed muon $g-2$ is driven to a corner with such constraints.

Reference [35] proposed augmenting the type-X 2HDM with another inert scalar doublet with the aim to enlarge the parameter region compatible with muon $g-2$. The resulting framework was dubbed as the $(2+1)$HDM. The scalars emerging from the inert multiplet were shown to induce sizeable contributions to muon $g-2$ through two-loop Barr-Zee (BZ) amplitudes. Such large amplitudes were shown to be consistent with various constraints from theory and experiments such as perturbative unitarity, Higgs signal strengths, and dark matter direct detection. It was established that the region in the M_A-$\tan\beta$ plane corroborating the observed muon $g-2$ and other constraints enlarges significantly upon the introduction of the inert scalar doublet. In this study, we perform a similar exercise for the muon-specific variant [36–38] of the $(2+1)$HDM, i.e., where the muons have enhanced Yukawa couplings while the taus have suppressed ones. We dub the $(2+1)$HDM with the type-X texture as introduced in [35] as a lepton-specific $(2+1)$HDM in this study, for clarity.

What phenomenologically sets apart the $(2+1)$HDM from the type-X 2HDM from the perspective of muon $g-2$ is the possibility of having a heavy pseudoscalar. And this can lead to interesting collider signatures through the $A \to \tau^+\tau^-$ decay. A heavier pseudoscalar would accordingly lead to more boosted $\tau^+\tau^-$ pair. Also, a final state involving the dark matter (DM) candidate η_R can have a very different spectrum of missing transverse energy ($\not{E}_T$) compared the SM or even the type-X 2HDM. With such considerations, we probed the signal $pp \to \eta_R\eta_I \to \eta_R\eta_R A \to \tau^+\tau^- + \not{E}_T$ at the 14 TeV LHC in [35]. Fully hadronic decays of the $\tau^+\tau^-$ pair were looked at. Encouraged by the ensuing results, in this work, we take up to probe the $e^+e^- \to \eta_R\eta_I \to \eta_R\eta_R A \to \tau^+\tau^- + \not{E}_T$ signal at the proposed

[*] nabarunc@iitk.ac.in
[†] indranic@iitk.ac.in
[‡] indrani300888@gmail.com

Published by the American Physical Society under the terms of the Creative Commons Attribution 4.0 International license. Further distribution of this work must maintain attribution to the author(s) and the published article's title, journal citation, and DOI. Funded by SCOAP³.

International Linear Collider (ILC) operating at $\sqrt{s} = 1$ TeV. We aim to explore all three possibilities: (i) both τ decay leptonically, (ii) one τ decays leptonically and the other hadronically, and (iii) both τ decay hadronically. An e^+e^- collider is expected to offer a higher sensitivity in probing a hadronic final state than what does the LHC given the tiny hadronic background in the former compared to in the latter. As for the muon-specific $(2+1)$HDM, the $A \to \mu^+\mu^-$ decay mode can have a sizeable branching ratio. Therefore, the channel we choose to investigate for this case is $e^+e^- \to \eta_R\eta_I \to \eta_R\eta_R A \to \mu^+\mu^- + \not{E}_T$. We plan to analyze the signals and the backgrounds using sophisticated multivariate techniques.

The study is structured as follows. We describe the details of the framework in Sec. II. The relevant theoretical and experimental constraints are discussed briefly in Sec. III. The same section also outlines explanation of the muon $g-2$ anomaly in the present setup. In Sec. IV, we present exhaustive analyses of the aforementioned signals using multivariate techniques. Finally, we summarize and conclude in Sec. V.

II. THEORETICAL FRAMEWORK: THE $(2+1)$HDM

The $(2+1)$HDM [35] is an extension of the 2HDM, comprising the scalar doublets ϕ_1 and ϕ_2, by an additional scalar doublet η. A $\mathbb{Z}_2'$ symmetry is imposed under which $(\phi_1, \phi_2) \to (\phi_1, \phi_2)$, while $\eta \to -\eta$. We quote below the most general scalar potential compatible with the gauge and discrete symmetries,

$$V(\phi_1, \phi_2, \eta) = V_2^{\{\phi_1,\phi_2,\eta\}} + V_4^{\{\phi_1,\phi_2\}} + V_4^{\{\phi_1,\phi_2,\eta\}}, \quad (2)$$

with

$$\begin{aligned}
V_2^{\{\phi_1,\phi_2,\eta\}} &= -m_{11}^2|\phi_1|^2 - m_{22}^2|\phi_2|^2 + m_{12}^2(\phi_1^\dagger\phi_2 + \text{H.c.}) + \mu^2|\eta|^2,\\
V_4^{\{\phi_1,\phi_2\}} &= \frac{\lambda_1}{2}|\phi_1|^4 + \frac{\lambda_2}{2}|\phi_2|^4 + \lambda_3|\phi_1|^2|\phi_2|^2 + \lambda_4|\phi_1^\dagger\phi_2|^2 + \frac{\lambda_5}{2}[(\phi_1^\dagger\phi_2)^2 + \text{H.c.}]\\
&\quad + \lambda_6[(\phi_1^\dagger\phi_1)(\phi_1^\dagger\phi_2) + \text{H.c.}] + \lambda_7[(\phi_2^\dagger\phi_2)(\phi_1^\dagger\phi_2) + \text{H.c.}],\\
V_4^{\{\phi_1,\phi_2,\eta\}} &= \frac{\lambda'}{2}|\eta|^4 + \sum_{i=1,2}\left\{\nu_i|\phi_i|^2|\eta|^2 + \omega_i|\phi_i^\dagger\eta|^2 + \left[\frac{\kappa_i}{2}(\phi_i^\dagger\eta)^2 + \text{H.c.}\right]\right\}\\
&\quad + [\sigma_1|\eta|^2\phi_1^\dagger\phi_2 + \sigma_2\phi_1^\dagger\eta\eta^\dagger\phi_2 + (\sigma_3\phi_1^\dagger\eta\phi_2^\dagger\eta + \text{H.c.})]. \quad (3)
\end{aligned}$$

Here the subscripts in Eq. (2) denote the dimensions of the respective terms while the superscripts denote the scalar doublets involved. All parameters in Eq. (2) are taken to be real to avoid CP violation. The particle content of the scalar doublets after electroweak symmetry breaking (EWSB) can be expressed as

$$\phi_i = \begin{pmatrix} \phi_i^+ \\ \frac{1}{\sqrt{2}}(v_i + h_i + iz_i) \end{pmatrix}, \qquad (i = 1,2),$$
$$\eta = \begin{pmatrix} \eta^+ \\ \frac{1}{\sqrt{2}}(\eta_R + i\eta_I) \end{pmatrix}. \quad (4)$$

Here v_i denotes the vacuum expectation value (VEV) of doublet ϕ_i with $i = 1, 2$ and one defines $\tan\beta = \frac{v_2}{v_1}$. The scalar doublet η is therefore inert, its component scalars do not mix with those coming from ϕ_1 and ϕ_2 on account of the $\mathbb{Z}_2'$ symmetry. It then follows that the physical scalar spectrum from these two doublets is identical to the pure 2HDM. We mention for completeness that such a spectrum comprises the CP-even h, H, the CP-odd A, and one charged Higgs H^+. Of these, h is identified with the discovered Higgs having mass 125 GeV. We refer to [15] for details. On the other hand, the inert sector is composed of three scalars η_R, η_I, and η^+. Their masses in terms of quartic couplings and mixing angles can be found in [35].

For the Yukawa interactions, we take the two following cases: i.e., (i) lepton-specific [15–21,23,24,26–28], the quarks get their masses from ϕ_2 while the all the leptons do from ϕ_1, and (ii) muon-specific [36–39], the quarks and the e, τ leptons get their masses from ϕ_2 while the μ lepton does from ϕ_1. The lepton-specific case is canonically known as the type-X 2HDM. The Yukawa Lagrangian in either case can be expressed as

$$\begin{aligned}
-\mathcal{L}_Y &= y_u\overline{Q_L}\tilde{\phi}_2 u_R + y_d\overline{Q_L}\phi_2 d_R\\
&\quad + \sum_{\ell=e,\mu,\tau}\left[n_\ell^1 y_\ell\overline{Q_L}\phi_1\ell_R + n_\ell^2 y_\ell\overline{Q_L}\phi_2\ell_R\right] + \text{H.c.} \quad (5)
\end{aligned}$$

Here y_u, y_d, y_ℓ are the Yukawa coupling matrices for the up-type quarks, down-type quarks, and charged leptons, respectively. We have taken the entries of these Yukawa coupling matrices to be real to avoid CP violation. The integers n_ℓ^1 and n_ℓ^2 are tabulated in Table I for the lepton- and muon-specific cases. We can rewrite the Lagrangian for the leptonic part in Eq. (5) in terms of the physical scalars as

TABLE I. Leptonic scale factors for the lepton- and muon-specific cases.

	$n^1_{e,\tau}$	$n^2_{e,\tau}$	n^1_μ	n^2_μ	ξ^h_e	ξ^h_μ	ξ^h_τ	ξ^H_e	ξ^H_μ	ξ^H_τ	ξ^A_e	ξ^A_μ	ξ^A_τ
Lepton-specific	1	0	1	0	$-\frac{\sin\alpha}{\cos\beta}$	$-\frac{\sin\alpha}{\cos\beta}$	$-\frac{\sin\alpha}{\cos\beta}$	$\frac{\cos\alpha}{\cos\beta}$	$\frac{\cos\alpha}{\cos\beta}$	$\frac{\cos\alpha}{\cos\beta}$	$\tan\beta$	$\tan\beta$	$\tan\beta$
Muon-specific	0	1	1	0	$\frac{\cos\alpha}{\sin\beta}$	$-\frac{\sin\alpha}{\cos\beta}$	$\frac{\cos\alpha}{\sin\beta}$	$\frac{\sin\alpha}{\sin\beta}$	$\frac{\cos\alpha}{\cos\beta}$	$\frac{\sin\alpha}{\sin\beta}$	$-\cot\beta$	$\tan\beta$	$-\cot\beta$

$$\mathcal{L}_Y^{\rm lepton} = \sum_{\ell=e,\mu,\tau} \frac{m_\ell}{v}(\xi^h_\ell h\bar{\ell}\ell + \xi^H_\ell H\bar{\ell}\ell - i\xi^A_\ell A\bar{\ell}\gamma_5\ell + [\sqrt{2}\xi^A_\ell H^+\overline{\nu_\ell}P_R\ell + \text{H.c.}]). \tag{6}$$

In the above equation, m_ℓ is the mass of the lepton ℓ, P_R is the projection operator, i.e., $P_R = \frac{(1+\gamma_5)}{2}$. The various ξ_ℓ factors are also quoted in Table I for the lepton-specific and muon-specific cases. The corresponding scale factors for the quarks coincide with the canonical type-X and are therefore not repeated here.

III. CONSTRAINTS AND THE MUON $g-2$ ANOMALY

We first describe in a nutshell the constraints applicable on this framework. The scalar quartic couplings are subject to the theoretical requirements of perturbativity, unitarity, and a bounded-from-below scalar potential. Several crucial restrictions come from experiments. First, the electroweak oblique parameters S, T, U must lie within their stipulated limits [40]. Second, the framework must pass the Higgs signal strength constraints for various channels. In this study, we adhere to the 2HDM alignment limit in which tree-level couplings of h to fermions and gauge bosons become identical to the corresponding SM values. And the only nontrivial signal strength constraint in this limit comes from the $h\to\gamma\gamma$ channel. The oblique parameter and $h\to\gamma\gamma$ signal strength constraints are imposed at 2σ in this analysis.

The $\mathbb{Z}_2'$ symmetry used in this framework renders the lighter of η_R or η_I as a DM candidate. We take η_R to be the one in this analysis. However, instead of demanding that η_R entirely accounts for the observed DM relic density, we allow for DM underabundance in this scenario. That is, we demand that the predicted relic density of η_R should not exceed the latest Planck data at the 2σ level that reads $\Omega_{\rm Planck}h^2 = 0.120 \pm 0.001$ [41]. The DM relic density is computed in this study by sequentially using the publicly available tools LanHEP [42] and micrOMEGAs [43]. In addition, upper limits are put on DM-nucleon scattering rates by direct detection experiments with the most stringent bound for sub-TeV DM comes from XENON-1T [44].

Details of the calculation of Δa_μ can be found in [35] and are skipped here for brevity. For convenience, we have provided the mathematical expressions and corresponding Feynman diagrams of one-loop and two-loop Barr-Zee contributions to Δa_μ coming from BSM scalars occurring in the loop in the Appendix. We scan over the model parameters and filter out particular parameter points that are compatible with the theoretical and experimental constraints and also obey the observed muon $g-2$ anomaly. At the alignment limit, we consider the following parameters as independent in the $(2+1)$HDM framework: $\{m_{12}, M_H, M_A, M_{H^+}, M_{\eta_R}, M_{\eta_I}, M_{\eta^+}, \tan\beta, \alpha, \lambda_6, \lambda_7, \omega_1, \kappa_1, \sigma_1, \sigma_2, \sigma_3, \lambda_{L_1}, \lambda_{L_2}\}$, with $\lambda_{L_{1(2)}} = \nu_{1(2)} + \omega_{1(2)} + \kappa_{1(2)}$. To minimize the number of input parameters, we fix $M_H = M_{H^+} = 150$ GeV, $M_{\eta^+} = M_{\eta_R} + 1\ \text{GeV} = 100$ GeV,[1] and $\lambda_6 = \lambda_7 = \lambda_{L_{1(2)}} = 0.01$. Low mass splittings between the neutral and charged scalars are consistent with the T-parameter constraint. Other independent input parameters are varied as

$$\begin{aligned} &0 < m_{12} < 1\ \text{TeV}, \quad 20\ \text{GeV} < M_A < 1\ \text{TeV}, \\ &M_{\eta_R} + 1\ \text{GeV} \le M_{\eta_I} \le 500\ \text{GeV}, \\ &10 < \tan\beta < 100, \quad |\omega_1|, \\ &|\kappa_1| < 4\pi, \quad |\sigma_1|, \quad |\sigma_2|, \quad |\sigma_3| < 2\pi. \end{aligned} \tag{7}$$

We further fix $M_H = 150$ GeV and $M_{\eta^+} = M_{\eta_R} = 100$ GeV, similar to in [35]. Parameter points validated by all the constraints are plotted in the M_A-$\tan\beta$ plane in Fig. 1(a) [Fig. 1(b)] for the lepton-specific (muon-specific) $(2+1)$HDM. One can conclude that for both variants of 2HDM, the parameter space consistent with the observed muon anomaly in the $\tan\beta$ vs M_A plane is enlarged in presence of the inert sector (cyan region) with respect to a pure 2HDM (green region).

IV. COLLIDER ANALYSIS

In this section, we present exhaustive probes in context of a 1 TeV ILC of a signal topology arising in the $(2+1)$HDM. Before going to the details of the analysis, we reiterate that, compared to the pure type-X 2HDM, the $(2+1)$HDM allows for a heavier A that is consistent with the observed Δa_μ. Therefore, this finding motivates to probe these heavier pseudoscalars through their decays to $\tau^+\tau^-$ or $\mu^+\mu^-$.

In the companion paper [35], a signature involving the pair production of η_R, η_I, followed by their subsequent

[1]The minimum 1 GeV mass gap between η_R and η_I, η^+ prohibits W, Z-mediated inelastic direct detection scatterings.

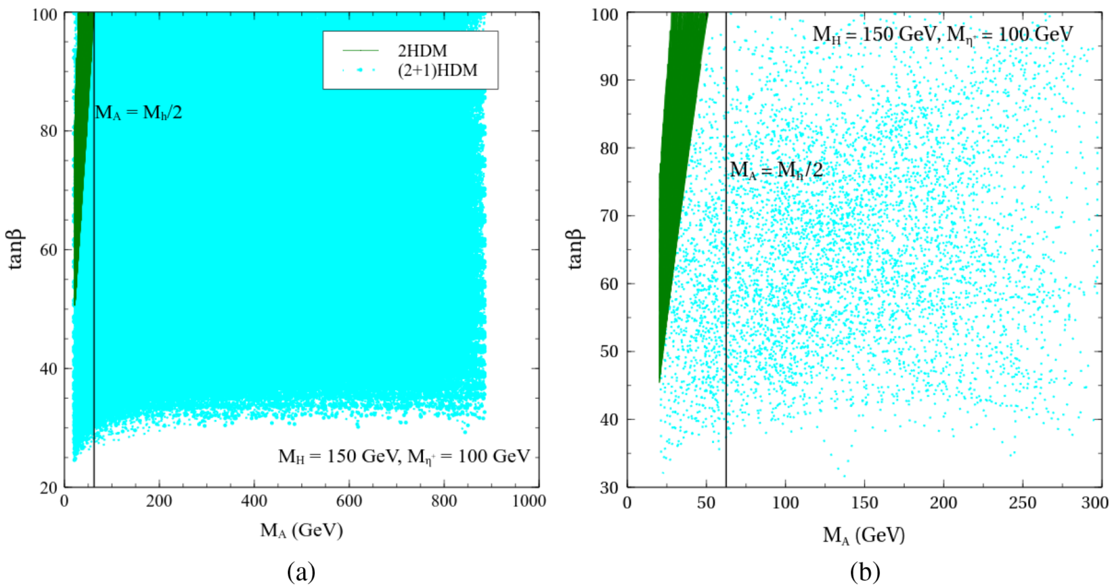

FIG. 1. The parameter space compatible with the observed Δa_μ in the M_A-$\tan\beta$ plane for $M_{\eta_R} = mM_{\eta^+} = 100$ GeV in case of (a) lepton-specific 2HDM and $(2+1)$HDM, (b) muon-specific 2HDM and $(2+1)$HDM. The color coding is explained in the legends. The region to the left of the vertical line is tightly constrained by $\mathrm{BR}(h \to AA)$ measurements. The plot in the left panel is taken from [35].

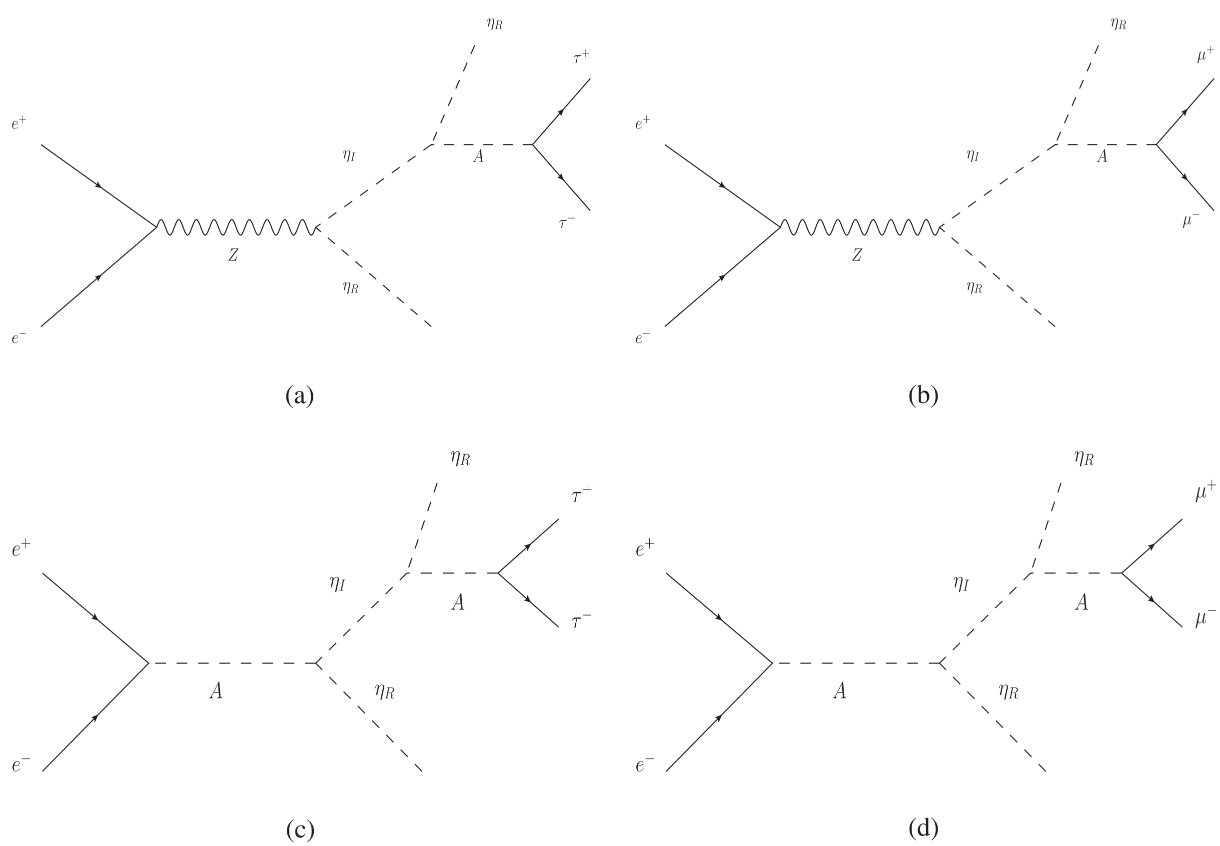

FIG. 2. Feynman diagrams for the signal channels: (a) for lepton specific $(2+1)$HDM mediated by Z, (b) for muon specific $(2+1)$HDM mediated by Z, (c) for lepton specific $(2+1)$HDM mediated by A, (d) for muon specific $(2+1)$HDM mediated by A.

TABLE II. Benchmark points used for studying the discovery prospects of an A in the lepton-specific $(2+1)$HDM. The values for the rest of the masses are $M_H = M_{H^+} = 150$ GeV, $M_{\eta^+} = M_{\eta_R} + 1$ GeV $= 100$ GeV.

	BP1	BP2	BP3	BP4
m_{12}	21.60 GeV	20.4 GeV	21.0 GeV	22.2 GeV
$\tan\beta$	47.8	53.83	50.77	45.46
M_A	152.3 GeV	253.24 GeV	353.20 GeV	404.16 GeV
M_{η_I}	270.5 GeV	397.00 GeV	492.0 GeV	547.0 GeV
k_1	−4.12177	−2.07345	−1.4954	−0.615752
ω_1	−5.50407	−0.125664	−5.93133	−2.01062
σ_1	−4.24743	−5.70513	−5.31557	−5.17734
σ_2	4.1469	−0.263894	5.81823	5.98159
σ_3	6.05699	5.44124	6.19522	6.06956
$\Delta a_\mu \times 10^9$	1.57538	1.51138	2.05397	1.85177
$\sigma_{SI}^{\rm eff}$	2.73×10^{-48} cm^2	3.81×10^{-50} cm^2	2.03×10^{-48} cm^2	2.96×10^{-48} cm^2
BR$(\eta_I \to \eta_R A)$	0.97475	0.822958	0.642342	0.513814
BR$(A \to \tau^+\tau^-)$	0.99	0.7983	0.199417	0.104883

decay into two τ hadrons (τ_h) along with missing transverse energy ($\not{E}_T$) was explored at the high-luminosity 14 TeV Large Hadron Collider (HL-LHC). We reckon that the same final state could turn out to be more promising at the ILC owing to the hadronically cleaner environment. We also plan to include the leptonic and semileptonic decay modes of τ to draw comparisons. Thus in this paper, we shall study the following channel for the lepton-specific $(2+1)$HDM.

$$e^+e^- \to \eta_R\eta_I \to \eta_R\eta_R A \to \tau^+\tau^- + \not{E}_T. \tag{8}$$

The following are the possibilities *vis-á-vis* τ decays:

(1) Both τ decay leptonically leading to the final state $2\tau_\ell + \not{E}_T$ with $\tau_\ell = \tau_e, \tau_\mu$.
(2) A semileptonic decay (one τ decays leptonically, another hadronically) leading to the final state $1\tau_\ell + 1\tau_h + \not{E}_T$.
(3) Both τ decaying hadronically leading to the final state $2\tau_h + \not{E}_T$. Here, τ_h denotes the visible hadronic decay product of the τ or a τ jet.

The branching ratio BR$(A \to \mu^+\mu^-)$ can be sizeable for the muon-specific $(2+1)$HDM despite the low muon mass. The signal we take up for this case is thus

$$e^+e^- \to \eta_R\eta_I \to \eta_R\eta_R A \to \mu^+\mu^- + \not{E}_T. \tag{9}$$

The $\eta_R\eta_I$ pair is produced through s-channel exchanges of Z and A. The Feynman diagrams for the lepton- and muon-specific cases are shown in Fig. 2.

In hindsight, we would like to make an overall comment on the choice of the signal topology. First, the $A \to \tau^+\tau^-, \mu^+\mu^-$ channels become the natural choices to look for A, given the healthy branching ratios and also the scope to identify the pseudoscalar mass. Second, involving the inert scalars in the signals should ultimately lead to a modified $\not{E}_T$ signature which in turn could be a discerning kinematical feature. We state the common parameter choices made in the lepton- and muon-specific cases. We take $M_H = M_{H^+} = 150$ GeV and $M_{\eta^+} = M_{\eta_I} + 1$ GeV $= 100$ GeV throughout the analyses. The subsequent collider analysis is divided into the following two subsections for clarity.

A. Signatures in the lepton-specific case

We propose a few benchmark points (BP1–4 in the increasing order of M_A) in Table II for the lepton-specific case. All four BPs are consistent with the constraints imposed and predict Δa_μ in the 2σ band. One further notes that $M_{\eta_I} > M_{\eta_R} + M_A$ holds for all the BPs so that the $\eta_I \to \eta_R A$ mode is kinematically open. M_{η_I} increases in going from BP1 to BP4 and branching fractions for the $\eta_I \to \eta_R Z, \eta^\pm W^\mp$ modes accordingly increase thereby explaining the observed drop in the $\eta_I \to \eta_R A$ branching ratio. We discuss the decays of A next. While $A \to \tau^+\tau^-$ is the dominant mode for BP1, the larger values of M_A taken for BP2–4 imply that $A \to ZH, W^\pm H^\mp$ also open up. And BR$(A \to \tau^+\tau^-)$ thus diminishes accordingly.

We now discuss the possible backgrounds for hadronic, semileptonic and leptonic decays of the $\tau^+\tau^-$ pair. First, $e^+e^- \to \tau^+\tau^- + \not{E}_T$ can be a common source of background in all the three cases. The dominant contributors to a $\tau^+\tau^- + \not{E}_T$ process are these: $W^+W^-(W^+ \to \tau^+\nu_\tau, W^- \to \tau^-\bar{\nu}_\tau)$, $ZZ(Z \to \tau^+\tau^-, Z \to \nu_\tau\bar{\nu}_\tau)$, $W^+W^-Z(W^+ \to \tau^+\nu_\tau, W^- \to \tau^-\bar{\nu}_\tau, Z \to \nu_\tau\bar{\nu}_\tau)$, $ZZZ(Z \to \tau^+\tau^-, Z \to \nu_\tau\bar{\nu}_\tau, Z \to \nu_\tau\bar{\nu}_\tau)$, $Zh(h \to \tau^+\tau^-, Z \to \nu_\tau\bar{\nu}_\tau)$. In addition, one also needs to consider $e^+e^- \to 2j + \not{E}_T$ and $e^+e^- \to \ell^+\ell^- + \not{E}_T$, where j denotes a light jet and $\ell = e, \mu$. The former is important while analyzing $2\tau_h + \not{E}_T$ since light jets can get mistagged as τ hadrons. On the other hand, $\ell^+\ell^- + \not{E}_T$

TABLE III. Signal and background cross sections for lepton specific $(2+1)$HDM at the 1 TeV ILC.

Signal/ Backgrounds	Process	P0 (fb)	P1 (fb)	P2 (fb)	P3 (fb)
Signal					
BP1		8.687	12.6	8.23	10.045
BP2	$e^+e^- \to \eta_R\eta_I \to \eta_R\eta_R A \to \tau^+\tau^- + \not{E}_T$	4.992	6.42	4.14	5.125
BP3		0.645	0.9	0.57	0.707
BP4		0.2118	0.29	0.189	0.235
Background	$e^+e^- \to \tau^+\tau^- + \not{E}_T$	55.76	127.9	12.26	9.405
	$e^+e^- \to 2j + \not{E}_T$	414.6	949.8	96.78	76.94
	$e^+e^- \to 2\ell + \not{E}_T$	419.0	915.2	115.8	89.34

becomes the principal background for analyzing the $2\tau_\ell + \not{E}_T$ final state. The dominant contributors to this background are these: $W^+W^-(W^+ \to \ell^+\nu_\ell, W^- \to \ell^-\bar{\nu}_\ell)$, $ZZ(Z\to\ell^+\ell^-, Z\to\nu_\ell\bar{\nu}_\ell)$, $W^+W^-Z(W^+\to\ell^+\nu_\ell, W^-\to\ell^-\bar{\nu}_\ell, Z\to\nu_\ell\bar{\nu}_\ell)$, $ZZZ(Z\to\ell^+\ell^-, Z\to\nu_\ell\bar{\nu}_\ell, Z\to\nu_\ell\bar{\nu}_\ell)$, $Zh(h\to\ell^+\ell^-, Z\to\nu_\ell\bar{\nu}_\ell)$ etc. Finally, in an e^+e^- environment, possible backgrounds to $1\tau_h + 1\tau_\ell + \not{E}_T$ can come only through mistagging. This might include a τ_h from $2\tau_h + \not{E}_T$ faking as an ℓ or an ℓ from $2\tau_\ell + \not{E}_T$ getting misidentified as a τ_h.

We display the signal and background cross sections at the leading order (LO) for unpolarized (P0) and polarized (P1, P2, P3) e^+ and e^- beams in Table III. The polarizations P1, P2, P3 are defined as follows [45]:

P1 ≡ 80% left-handed e^- and 30% right-handed e^+ beam $(P_{e^-}, P_{e^+} = 80\%L, 30\%R)$.

P2 ≡ 80% right-handed e^- and unpolarized e^+ beam $(P_{e^-}, P_{e^+} = 80\%R, 0)$.

P3 ≡ 80% right-handed e^- and 30% left-handed e^+ beam $(P_{e^-}, P_{e^+} = 80\%R, 30\%L)$.

The relevant interaction vertices of the $(2+1)$HDM setup are first implemented in FeynRules [46]. The resulting Universal FeynRules Output (UFO) file is passed over to MG5AMC@NLO [47,48] for the generation of signal and backgrounds at the leading order. Showering and hadronization are incorporated through PYTHIA8 [49]. Finally, detector effects are included in the analysis via passing the signal and backgrounds through Delphes-3.4.1 [50]. For this purpose, we use the default ILD detector simulation card present in Delphes-3.4.1. To obtain the best possible results we refrain from doing a traditional cut-based analysis but rather perform the more sophisticated multivariate analysis using Decorrelated Boosted Decision Tree (BDTD) algorithm embedded in the Toolkit for Multivariate Data Analysis [51] platform. We refer to [51] for the detailed description of this algorithm. The signal significance is computed using $\mathcal{S} = \sqrt{2[(S+B)\log(\frac{S+B}{B}) - S]}$, where S and B are the number of signal and background events left after imposing cuts on pertinent kinematic variables [52]. The following cuts are imposed at the level of event generation:

$$p_T^j > 20 \text{ GeV}, \qquad |\eta_j| < 5.0,$$
$$p_T^\ell > 10 \text{ GeV}, \qquad |\eta_\ell| < 2.5,$$
$$\Delta R_{mn} > 0.4, \quad \text{where } m, n = \ell, \text{jets}. \tag{10}$$

Here $p_T^{j(\ell)}$ and $|\eta_{j(\ell)}|$ denote the transverse momentum and pseudorapidity of the final state jets (leptons), respectively. One defines $\Delta R_{mn} = \sqrt{\Delta\eta_{mn}^2 + \Delta\phi_{mn}^2}$, $\Delta\eta_{mn}$, and $\Delta\phi_{mn}$ being the difference between pseudorapidity and azimuthal angles of mth and nth particles, respectively.

To avoid repetition, we shall only tabulate some relevant parameters used in the BDTD algorithm for all channels. A naive estimation of the signal-to-background ratio at this level (from Table III) for all the polarizations shows P3 to be the most prospective in this regard. Therefore, we pick up P3 for the multivariate analyses in case of all the final states. The analyses for the three cases is divided into the three following subsections for clarity.

1. $2\tau_\ell + \not{E}_T$ *final state*

The two τ decay leptonically lead to $\tau_{e^+}\tau_{e^-}, \tau_{e^\pm}\tau_{\mu^\mp}, \tau_{\mu^+}\tau_{\mu^-}$ along with $\not{E}_T$. We denote the two daughter leptons to be ℓ_1 and ℓ_2 in the decreasing order of their p_T. The following kinematic variables are used while training the signal and background samples using the BDTD algorithm:

$$\Delta\phi_{\ell_1\ell_2}, \quad \Delta\phi_{\ell_2\not{E}_T}, \quad \Delta R_{\ell_1\ell_2}, \quad \eta_{\ell_1}, \quad \not{E}_T,$$
$$M_{\ell_1\ell_2}, \quad M_T^{\rm vis}(\ell_1,\ell_2), \quad p_T^{\ell_1}.$$

We define the aforementioned kinematic variables for completeness. Here, $\Delta\phi_{\ell_1\ell_2}(\Delta\phi_{\ell_2\not{E}_T})$ is the difference in azimuthal angles between ℓ_1, ℓ_2 (ℓ_2 and the missing transverse energy vector $\not{E}_T$) in the final state. While $M_{\ell_1\ell_2}$ is the invariant mass of the two daughter leptons, $M_T^{\rm vis}(\tau_{\rm vis1},\tau_{\rm vis2})$ is the cluster transverse mass [53] that can be constructed out of the visible decay products of the $\tau(\tau_{\rm vis1},\tau_{\rm vis2})$ in the final state and $\not{E}_T$ as follows:

$$\begin{aligned}[M_T^{\rm vis}(\tau_{\rm vis1},\tau_{\rm vis2})]^2 &= \left(\sqrt{|\vec{p}_T(\tau_{\rm vis1},\tau_{\rm vis2})|^2 + M(\tau_{\rm vis1},\tau_{\rm vis2})^2} + \not{E}_T\right)^2 \\ &\quad - (\vec{p}_T(\tau_{\rm vis1},\tau_{\rm vis2}) + \vec{\not{E}}_T)^2.\end{aligned} \tag{11}$$

Here $M(\tau_{\rm vis1},\tau_{\rm vis2})$ and $\vec{p}_T(\tau_{\rm vis1},\tau_{\rm vis2})$ are the invariant mass and the vector transverse momentum of the two visible τ decays, respectively. We note that $M_T^{\rm vis}(\tau_{\rm vis1},\tau_{\rm vis2})$ becomes relevant when there is more than one source of missing transverse energy and the collinear approximation [54] is no longer valid. As discussed earlier, the main background in this case comes from $e^+e^- \to \ell^+\ell^- + \not{E}_T$

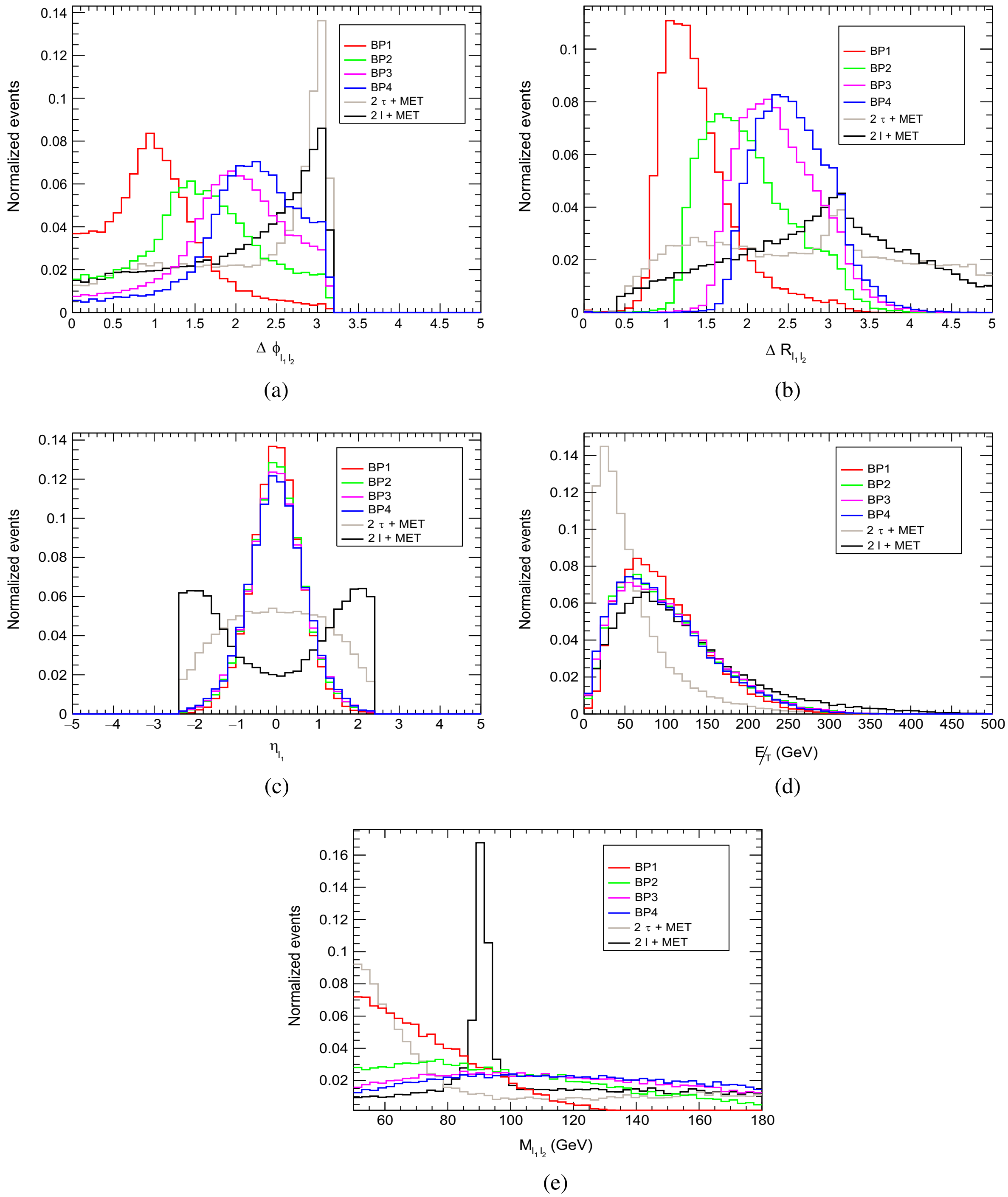

FIG. 3. Normalized distributions of $\Delta\phi_{\ell_1\ell_2}, \Delta R_{\ell_1\ell_2}, \Delta\phi_{\ell_2 \not{E}_T}, \eta_{\ell_1}, \not{E}_T, M_{\ell_1\ell_2}$ for $2\tau_\ell + \not{E}_T$ channel at 1 TeV ILC.

with a subleading component contributed by $e^+e^- \to \tau^+\tau^- + \not{E}_T$ when both τ decay leptonically. Figures 3 and 4 show normalized distributions of the most important variables for the signal BPs and the backgrounds.

Figures 3(a) and 3(b) display the normalized distributions of $\Delta\phi_{\ell_1\ell_2}$ and $\Delta R_{\ell_1\ell_2}$, respectively. Since, for the signal, the two τ originate from a single mother particle A, the daughter leptons ℓ_1, ℓ_2 are not as widely separated as in case of the backgrounds. Thus the distributions of $\Delta\phi_{\ell_1\ell_2}$ and $\Delta R_{\ell_1\ell_2}$ for the four signal BPs peak at lower values compared to the backgrounds. However, the larger the M_A, the higher the $\Delta R_{\ell_1\ell_2}$ value is where the signal distribution peaks. This can be understood from the fact that a lighter A would be somewhat more boosted than a heavier A. And the decay products of a more boosted object would be more collimated accordingly. Thus the observed pattern in $\Delta\phi_{\ell_1\ell_2}$ and $\Delta R_{\ell_1\ell_2}$ for BP1 to BP4.

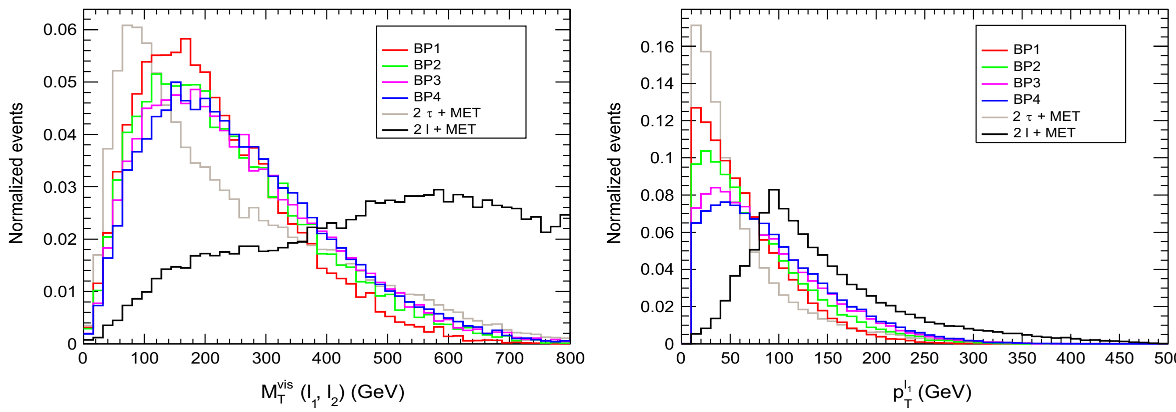

(a) (b)

FIG. 4. Normalized distributions of $M_T^{\text{vis}}(\ell_1, \ell_2)$, $p_T^{\ell_1}$ for $2\tau_\ell + \not{E}_T$ channel at 1 TeV ILC.

In Fig. 3(c), we have drawn the pseudorapidity distribution of the leading lepton ℓ_1. It is seen that this distribution peaks at zero for both signal and the $2\tau + \not{E}_T$ background. Such a semblance is expected given ℓ_1 comes from a τ in all such cases. On the other hand, the $2\ell + \not{E}_T$ background is a more inclusive process involving s-channel exchanges of γ, Z, and a t-channel exchange of νs. Thus, owing to the different kinematics of this background, the η_{ℓ_1} distribution accordingly is different with two peaks placed symmetrically about zero. We also point out that the invariant mass ($M_{\ell_1\ell_2}$) distribution for $2\ell + \not{E}_T$ background in Fig. 3(e) has a sharp peak around Z-boson mass M_Z. This is due to the fact that a contributor to the $2\ell + \not{E}_T$ background is with the two Z decaying to $\ell\bar{\ell}$ and $\nu\bar{\nu}$. Normalized distributions of $p_T^{\ell_1}$ and $\not{E}_T$ are shown in Figs. 4(b) and 3(d). The leading lepton ℓ_1 is seen to be more boosted in the case of the $2\ell + \not{E}_T$ background. This can be attributed to the fact that ℓ_1, ℓ_2 in this case are produced directly through s- and t-channel scatterings. The next hardest $p_T^{\ell_1}$ spectrum is that of the signal BP4. It is expected that the heavier the decaying pseudoscalar, the more boosted are the daughter τ leptons. This is why the peak of $p_T^{\ell_1}$ distribution progressively shifts towards lower values from BP4 to BP1. The softest distribution of all is that of the $2\tau_\ell + \not{E}_T$ background where the leptons come from τ decay only.

Neutrinos are the only source of missing transverse energy for the backgrounds. The neutrinos are the most boosted for the $2\ell + \not{E}_T$ background since these come from W and Z decays. Hence, the hardest-of-all $\not{E}_T$ spectrum is seen in the case of the $2\ell + \not{E}_T$ background. However, the low p_T neutrinos coming from the τ decays contaminate the sample in the case of the $2\tau_\ell + \not{E}_T$ background and hence the soft distribution is observed. The $\not{E}_T$ distribution for the signals is a measure of how boosted the undetected η_R is and the events peak around $p_T^{\eta_R} \sim \frac{(M_{\eta_I}^2 - M_A^2)}{2M_{\eta_R}}$. It is inferred for the M_{η_I} and M_A values for BP1–4 that the peaks of the $\not{E}_T$ distribution for these benchmarks are not far apart from one another. Overall, the $\not{E}_T$ distribution in Fig. 3(e) for BP1–4 are harder than that of $2\tau_\ell + \not{E}_T$ to an extent. In Figs. 3(c) and 4(b), normalized distributions of $\Delta\phi_{\ell_2 \not{E}_T}$ and $M_T^{\text{vis}}(\ell_1, \ell_2)$ are drawn. The $M_T^{\text{vis}}(\ell_1, \ell_2)$ distribution for the $2\ell + \not{E}_T$ background peaks at $\gtrsim 550$ GeV and is therefore in contrast with the signal BPs that peak at $\lesssim 200$ GeV.

Having described the primary features of the kinematic distributions, we now proceed to perform the BDTD analysis. We refer to [51] for details of the BDTD methodology. Different BDTD parameters like NTrees, MinNodesize, MaxDepth, nCuts, and Kolmogorov-Smirnov (KS) scores (for signal and backgrounds) for each benchmark are presented in Table IV. One can stabilize the KS scores simultaneously for signals and backgrounds upon tuning these parameters.

To get an idea on the efficiency of distinguishing signals from backgrounds, one can plot background rejection against signal efficiency for the BPs in what is called the receiver's operative characteristic (ROC) curve. From Fig. 5(a), one can see that the background rejection is maximum for BP1 and minimum for BP4. This pattern will be reflected while computing the signal significance, as we

TABLE IV. Tuned BDT parameters for BP1, BP2, BP3, BP4 for the $2\tau_\ell + \not{E}_T$ channel.

	NTrees	MinNode Size (%)	Max Depth	nCuts	KS-score for Signal (Background)
BP1	120	3	2.0	55	0.661 (0.119)
BP2	110	3	2.0	50	0.579 (0.023)
BP3	120	4	2.0	55	0.134 (0.908)
BP4	120	4	2.0	55	0.104 (0.315)

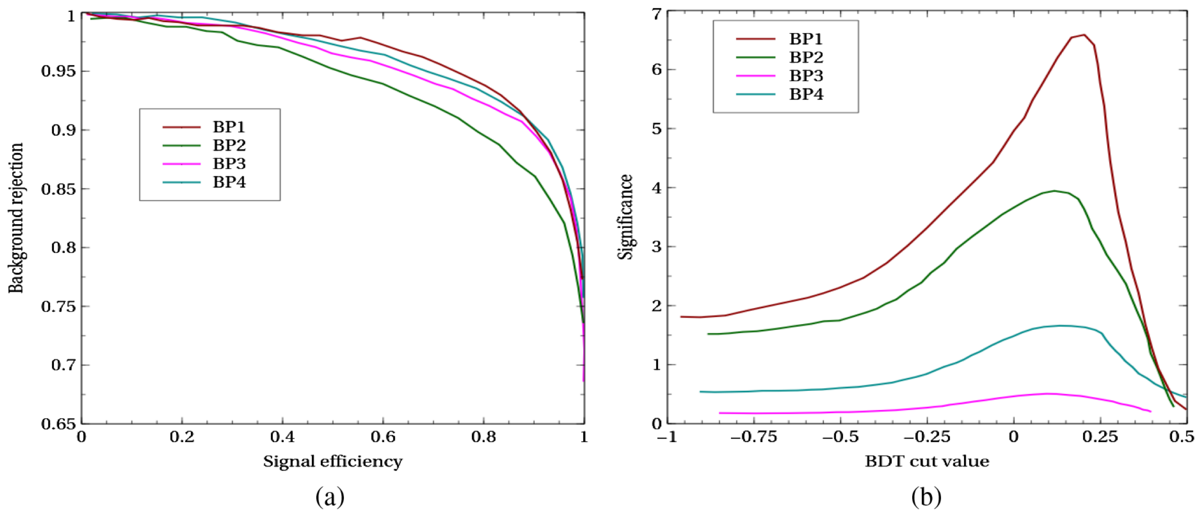

FIG. 5. (a) ROC curves for chosen benchmark points for $2\tau_\ell + \not{E}_T$ channel. (b) BDT scores corresponding to BP1, BP2, BP3, and BP4 for the $2\tau_\ell + \not{E}_T$ channel.

shall see shortly. Next to achieve maximum possible significance, we have to regulate the BDT cut value or the BDT score. Figure 5(b) depicts the variation of significance with BDT cut value. For different signal benchmarks, the significance attains the maximum value for a particular BDT score.

In Table V, we have tabulated the signal and the background yields at a reference integrated luminosity 1000 fb^{-1}. In the same table we quote the luminosity required to achieve a 5σ significance for each BP. The maximum observability is obtained for BP1. In fact, an $M_A \simeq 250$ GeV in BP2 is also found within the reach of the proposed 1000 fb^{-1} integrated luminosity. Higher M_A values however remain beyond this reach.

2. $1\tau_\ell + 1\tau_h + \not{E}_T$ final state

The main background in this case is the common process $e^+e^- \to \tau^+\tau^- + \not{E}_T \to 1\tau_\ell + 1\tau_h + \not{E}_T$. Given the minuscule $j \to \tau_h$ and $j \to \ell$ misidentification rates in an e^+e^- environment, we find that the contributions of $e^+e^- \to \ell^+\ell^- + \not{E}_T$ and $e^+e^- \to jj + \not{E}_T$ backgrounds become negligible in this case. We denote the lepton coming from the decay of one τ lepton as ℓ_1 and the τ hadron as τ_{h_1}.

TABLE V. The signal and background yields obtained using the BDTD analysis at 1 TeV ILC with 1000 fb^{-1} integrated luminosity corresponding to the signal BPs for the $e^+e^- \to 2\tau_\ell + \not{E}_T$ channel.

Benchmark point	Signal yield at 1000 fb^{-1}	Background yield at 1000 fb^{-1}	$\mathcal{L}_{5\sigma}$ (fb^{-1})
BP1	349	603	146
BP2	267	3790	1366
BP3	32	2150	$\sim 5.4 \times 10^4$
BP4	27	2677	$\sim 3.8 \times 10^5$

Following are the kinetic variables used for the multivariate analysis:

$$M_{\ell_1\tau_{h_1}},\ \not{E}_T,\ p_{T\,\ell_1\tau_{h_1}}^{\rm vect},\ M_T^{\rm vis}(\ell_1,\tau_{h_1}),\ \eta_{\ell_1},\ \Delta\phi_{\ell_1\tau_{h_1}},\ p_T^{\ell_1\tau_{h_1}},$$
$$\Delta R_{\ell_1\tau_{h_1}},\ p_T^{\tau_{h_1}},\ \Delta\eta_{\ell_1\tau_{h_1}},\ \Delta\phi_{\ell_1\not{E}_T},\ \Delta\phi_{\tau_{h_1}\not{E}_T},\ \eta_{\tau_{h_1}}. \tag{12}$$

We define some of the variables not defined earlier. The invariant mass of the ℓ_1 and τ_{h_1} in the final state is $M_{\ell_1\tau_{h_1}}$. Next, $p_{T\,\ell_1\tau_{h_1}}^{\rm vect}$, $p_T^{\ell_1\tau_{h_1}}$, and $p_T^{\tau_{h_1}}$ are the vector sum of the transverse momenta of ℓ_1 and τ_{h_1}, scalar sum of the transverse momenta of ℓ_1 and τ_{h_1} and transverse momentum of the τ_{h_1}, respectively. As mentioned in Sec. IVA 1, $M_T^{\rm vis}(\ell_1,\tau_{h_1})$ can be defined following Eq. (10), where two visible decay products of the two τ leptons are ℓ_1 and τ_{h_1} for the present channel. The definition of the other variables can be understood from their notation and the previous subsection can also be referred to for clarification.

Among the aforementioned important variables used in BDTD analysis, we present the normalized distributions of $\Delta\phi_{\ell_1\tau_{h_1}}$, $\Delta R_{\ell_1\tau_{h_1}}$, $\not{E}_T$, and $M_T^{\rm vis}(\ell_1,\tau_{h_1})$ in Figs. 6(a)–6(d) for the signal and backgrounds. The distributions of $\Delta\phi_{\ell_1\tau_{h_1}}$, $\Delta R_{\ell_1\tau_{h_1}}$ for signal benchmarks peak at lower values, whereas the background distribution has a peak at higher values in Figs. 6(a) and 6(b). The reason lies in the fact that the two final state particles (ℓ_1 and τ_{h_1}) from a single parent particle A for signal and hence are more collimated. The nature of the $\not{E}_T$ distribution has already been explained in Sec. IVA 1. From Fig. 6(d), one also reads that the $M_T^{\rm vis}(\ell_1,\tau_{h_1})$ distribution progressively becomes harder from BP1 to BP4. That is, the higher M_A is, the higher the value is where the distribution peaks. Given the soft distribution of the background, this variable is thus also important in separating the signal from the background.

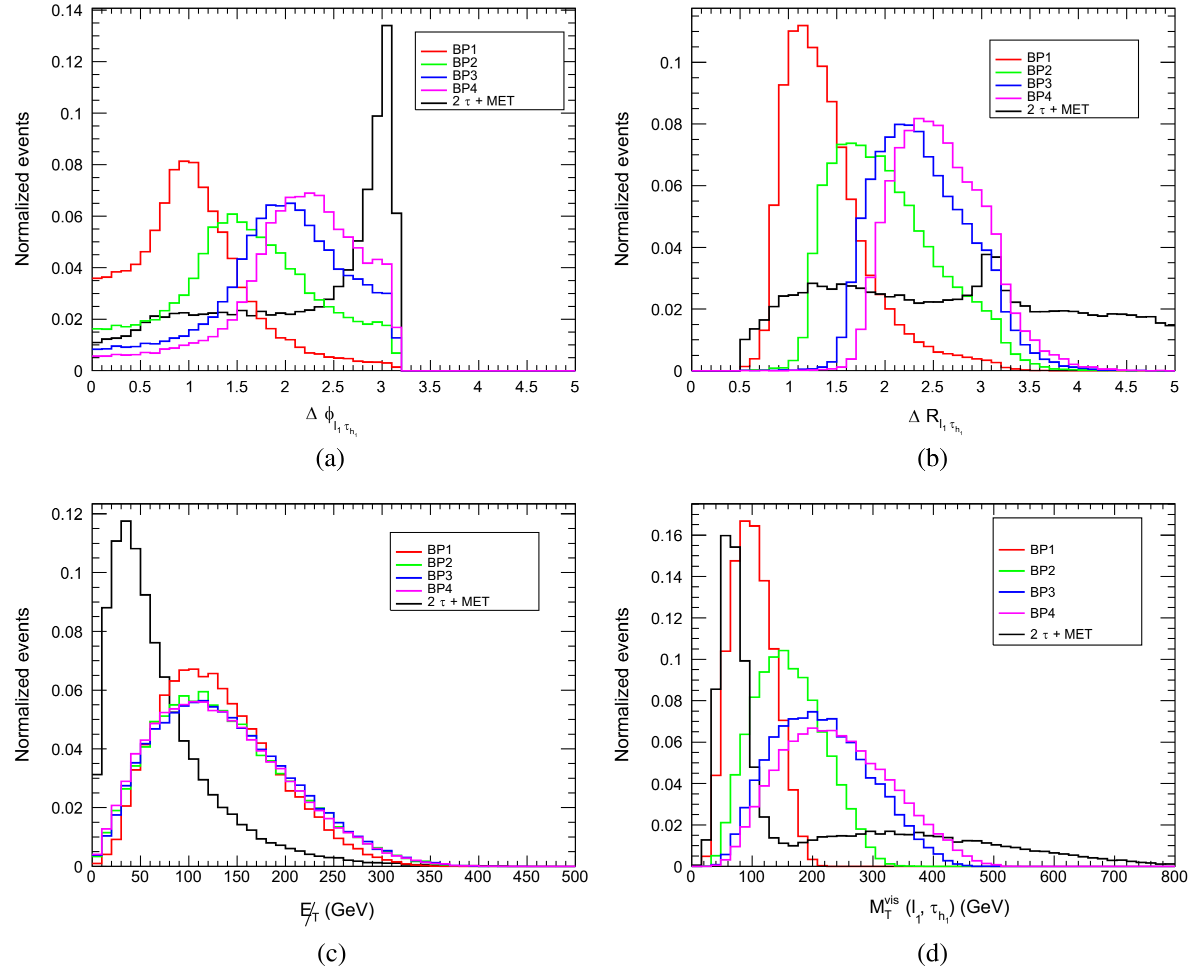

FIG. 6. Normalized distributions of $\Delta\phi_{\ell_1\tau_{h_1}}$, $\Delta R_{\ell_1\tau_{h_1}}$, $\not{E}_T$, $M_T^{\mathrm{vis}}(\ell_1, \tau_{h_1})$ for signal and backgrounds for the $1\tau_\ell + 1\tau_h + \not{E}_T$ final state.

We train the signal and background samples by adjusting the BDTD parameters (mentioned previously in Sec. IV A 1) tabulated in Table VI. The ROC curves and the variation of the significance with BDT score for this channel are depicted in Figs. 7(a) and 7(b), respectively. Figure 7(a) suggests that background rejection is the best for BP3 and BP4.

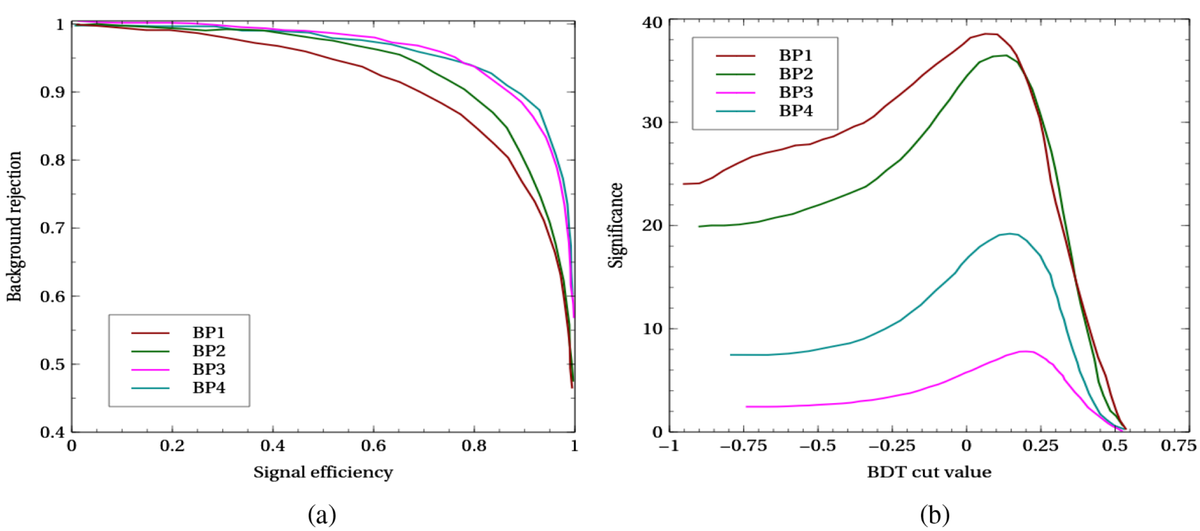

FIG. 7. (a) ROC curves for chosen benchmark points for $1\tau_\ell + 1\tau_h + \not{E}_T$ channel. (b) BDT scores corresponding to BP1, BP2, BP3, and BP4 for $1\tau_\ell + 1\tau_h + \not{E}_T$ channel.

TABLE VI. Tuned BDT parameters for BP1, BP2, BP3, BP4 for the $1\tau_\ell + 1\tau_h + \not{E}_T$ channel.

	NTrees	MinNodeSize (%)	MaxDepth	nCuts	KS-score for Signal (Background)
BP1	110	4	2.0	55	0.235 (0.378)
BP2	110	4	2.0	55	0.074 (0.363)
BP3	110	4	2.0	50	0.018 (0.304)
BP4	110	4	2.0	50	0.908 (0.131)

TABLE VII. The signal and background yields obtained using the BDTD analysis at 1 TeV ILC with 1000 fb^{-1} integrated luminosity corresponding to the signal BPs for the $e^+e^- \to 1\tau_\ell + 1\tau_h + \not{E}_T$ channel.

Benchmark Point	Signal Yield at 1000 fb^{-1}	Background Yield at 1000 fb^{-1}	$\mathcal{L}_{5\sigma}$ (fb^{-1})
BP1	836	114	11
BP2	462	61	5
BP3	50	15	69
BP4	13	32	1279

It is read from Table VII that the $1\tau_\ell + 1\tau_h + \not{E}_T$ channel comes with a 5σ discovery potential for M_A up to 350 GeV (BP1–3) within 300 fb^{-1} integrated luminosity. This is therefore a marked improvement with respect to the $2\tau_\ell + \not{E}_T$ channel.

3. $2\tau_h + \not{E}_T$ *final state*

We denote the hadronic decay products of the two τ leptons by τ_{h_1} and τ_{h_2}. The only sizeable background in this case too is $e^+e^- \to \tau^+\tau^- + \not{E}_T$ since $e^+e^- \to jj + \not{E}_T$, $\ell^+\ell^- + \not{E}_T$ have negligible effects, as explained in the previous subsection. The kinematic variables used for the BDTD analysis for this case are

$$\begin{aligned} &M_{\tau_{h_1}\tau_{h_2}}, \quad \not{E}_T, \quad p_{T\,\tau_{h_1}\tau_{h_2}}^{\mathrm{vect}}, \quad p_T{}^{\tau_{h_1}}, \\ &M_T{}^{\mathrm{vis}}(\tau_{h_1},\tau_{h_2}), \quad \eta_{\tau_{h_1}}, \quad \Delta\eta_{\tau_{h_1}\tau_{h_2}}, \quad \Delta\phi_{\tau_{h_1}\not{E}_T}, \\ &p_T^{\tau_{h_1}\tau_{h_2}}, \quad \Delta\phi_{\tau_{h_1}\tau_{h_2}}, \quad \Delta R_{\tau_{h_1}\tau_{h_2}}, \quad \eta_{\tau_{h_2}}, \\ &\Delta\phi_{\tau_{h_2}\not{E}_T}, \quad \phi_{\tau_{h_1}}, \quad \phi_{\tau_{h_2}}. \end{aligned} \tag{13}$$

Here $M_{\tau_{h_1}\tau_{h_2}}$ is the invariant mass of two τ jets in the final state. $p_{T\,\tau_{h_1}\tau_{h_2}}^{\mathrm{vect}}$, $p_T^{\tau_{h_1}\tau_{h_2}}$, $p_T{}^{\tau_{h_1}}$ are the vector and scalar sum of the transverse momenta of two τ jets, transverse momentum of the leading τ jet, respectively. Other variables are already defined earlier for different final states. Normalized distributions for $\Delta\phi_{\tau_{h_1}\tau_{h_2}}$, $\Delta R_{\tau_{h_1}\tau_{h_2}}$, $\not{E}_T$, $M_{\tau_{h_1}\tau_{h_2}}$, $M_T{}^{\mathrm{vis}}(\tau_{h_1},\tau_{h_2})$, $p_{T\tau_{h_1}}$ are presented in Figs. 8(a)–8(f), respectively.

The kinematical features seen can be understood from the discussions in the previous subsections. It is however mentioned for completeness that τ_{h_1}, τ_{h_2} are more collimated in case of the signals since they emerge from the decay of the pseudoscalar. Thus the particular distribution in Figs. 8(a) and 8(b). We also find in Fig. 8(c) that $\not{E}_T$ is a useful handle to discern the signal from the backgrounds for this channel too. The invariant mass and transverse mass of the $\tau_h\tau_h$ pair have somewhat correlated spectra, as seen in Figs. 8(d) and 8(e). And the discriminatory power of these variables increase with increasing M_A, a feature also seen for the $1\tau_\ell + 1\tau_h + \not{E}_T$ channel. The leading τ hadron is expectedly more boosted for a heavier pseudoscalar, as concurred by Fig. 8(f).

The signal and background KS scores for each BP are shown in Table VIII along with the corresponding tuned values of the BDTD variables. We also show the ROC curve and the significance vs BDT cut-value plot in Figs. 9(a) and 9(b), respectively. It is read from the ROC curve that background rejection is the least efficient for BP1. The efficiency enhances with increasing M_A albeit BP3 and BP4 are close by in this regard. We summarize the discovery prospects predicted by the BDTD analysis for the various BPs in Table IX. For the $\tau^+\tau^-$ pair decaying fully hadronically, BP1–3 can be discovered at 5σ within 375 fb^{-1}. In fact, BP4 is also found within the reach of the proposed 4000 fb^{-1} integrated luminosity.

We compare the efficacies of the $2\tau_\ell + \not{E}_T$, $1\tau_\ell + 1\tau_h + \not{E}_T$, and $2\tau_h + \not{E}_T$ channels before closing the discussion of the lepton-specific $(2+1)$HDM. It is readily seen that $2\tau_\ell + \not{E}_T$ is the least promising among the three. And this is attributed to two reasons. First, the leptonic decay of a τ has a smaller branching fraction than the hadronic one. More importantly, identification efficiency of the leptons coming from τ decays is poor in a realistic collider environment. The other two channels are mutually competing. For both, the BDTD training is the most efficiently trained to reject the background in the case of BP4. The quality of training becomes inferior for the BPs with lower values of M_A. While the semileptonic channel is found to be more promising in case of BP1–3, the hadronic channel is more efficient in case of BP4.

Lastly, we also compare the performances of the LHC and the ILC in looking for an A in the $2\tau_h + \not{E}_T$ final state. It is seen from [35] that an A of mass $\simeq$250 GeV can be observed at 5σ at the LHC when the integrated luminosity is around 3300 fb^{-1}. Therefore, the LHC discovery potential is considerably less compared to the ILC that predicts 5σ observability for $M_A \simeq 400$ GeV for an integrated luminosity around 3000 fb^{-1}. Therefore, this enhanced observability at the ILC is a clear upshot of the present

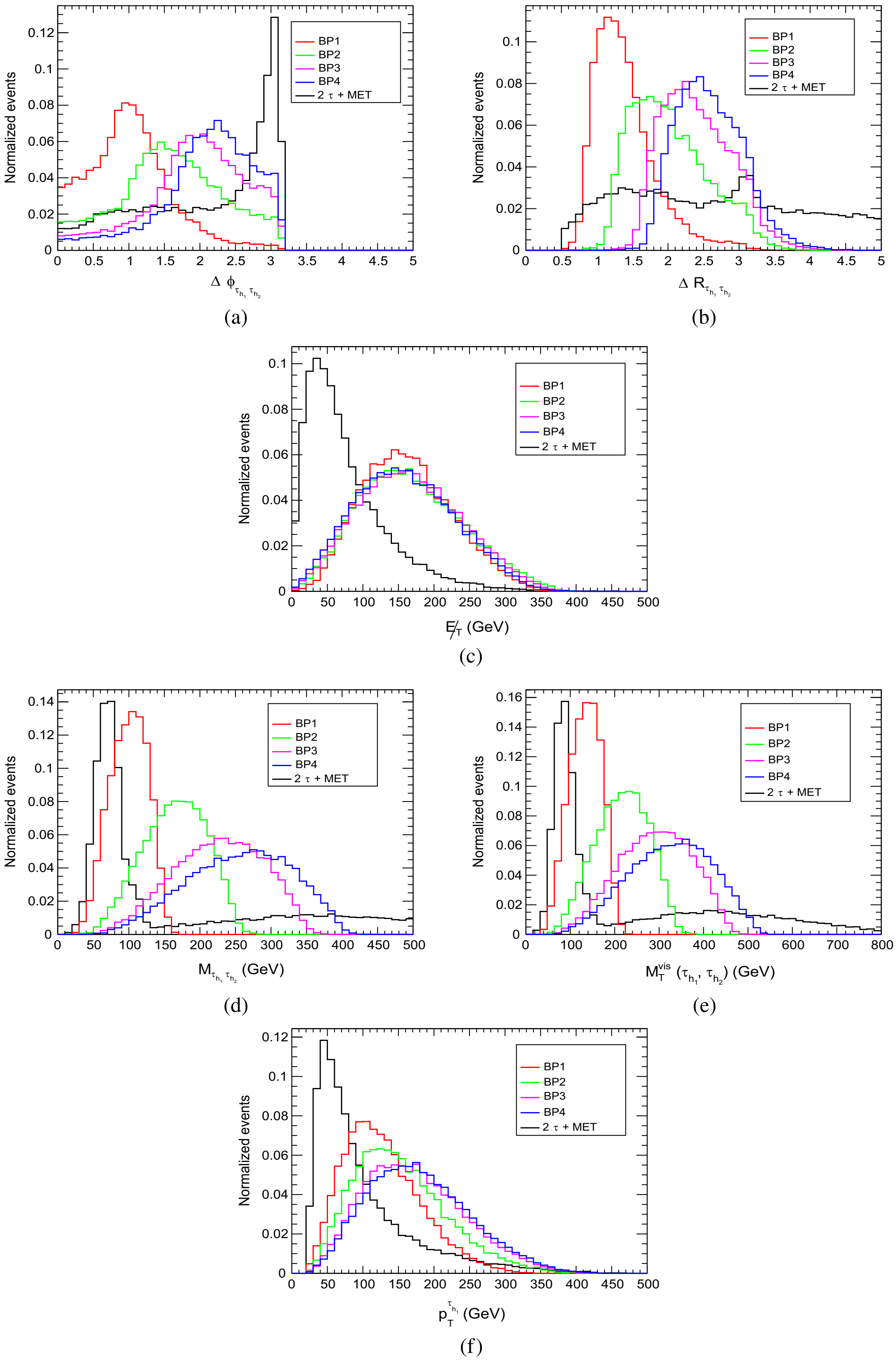

FIG. 8. Normalized distributions for $\Delta\phi_{\tau_{h_1}\tau_{h_2}}$, $\Delta\phi_{\tau_{h_2}\not{E}_T}$, $\Delta R_{\tau_{h_1}\tau_{h_2}}$, $\not{E}_T$, $M_{\tau_{h_1}\tau_{h_2}}$, $M_T{}^{\mathrm{vis}}(\tau_{h_1}, \tau_{h_2})$ for $2\tau_h + \not{E}_T$ channel at 1 TeV ILC.

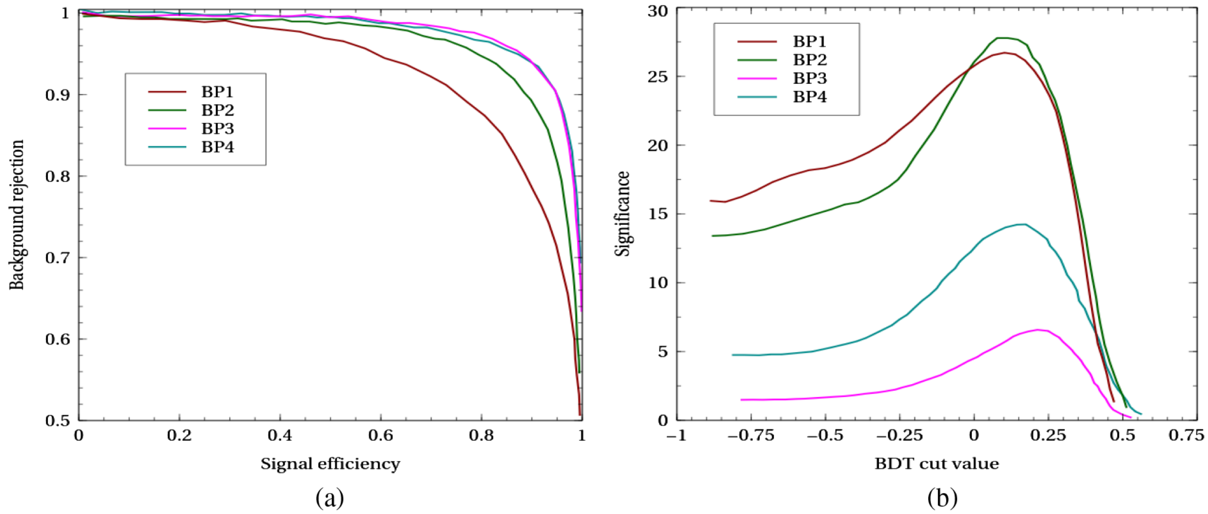

FIG. 9. (a) ROC curves for chosen benchmark points for $2\tau_h + \not{E}_T$ channel. (b) BDT scores corresponding to BP1, BP2, BP3, and BP4 for the $2\tau_h + \not{E}_T$ channel.

analysis. And this is attributed to the fact that hadronic background in a leptonic collider is minuscule compared to in a hadronic collider. And the former therefore would be generically more efficient in detecting hadronic activity stemming from a Beyond Standard Model (BSM) scenario, an example of which is the $e^+e^- \to \eta_R\eta_I \to \eta_R\eta_R A \to \tau^+\tau^- + \not{E}_T$ signal.

B. Muon specific 2HDM

We present two new sample points (SPs) in Table X for the muon-specific case from the corresponding allowed parameter region. It follows from the preceding discussions on the lepton-specific case that the most relevant background in the muon-specific case would be $e^+e^- \to \ell^+\ell^- + \not{E}_T$.

In Table XI, we have tabulated the signal cross sections (for SP1, SP2) along with the background cross section for the polarization configurations P3. The normalized distributions of $\not{E}_T, M_{\mu_1\mu_2}, p_T^{\mu_1\mu_2}, p_{T_{\mu_1\mu_2}}^{\rm vect}$ are shown in Figs. 10(a)–10(d), where μ_1 and μ_2 are p_T-ordered muons of the final state. Figure 10(b) shows that the invariant mass of the $\mu^+\mu^-$ pair for the signal BPs cleanly peaks around the corresponding M_A values. The signals thus have practically no overlap with the background as far as $M_{\mu_1\mu_2}$ is concerned. This is an important point of difference from the $\tau^+\tau^- + \not{E}_T$ signal in the lepton-specific $(2+1)$HDM in which case the invariant masses of the $\tau_{\ell_1}\tau_{\ell_2}$, $\tau_{\ell_1}\tau_{h_1}$, and

TABLE VIII. Tuned BDT parameters for BP1, BP2, BP3, BP4 for the $2\tau_h + \not{E}_T$ channel.

	NTrees	MinNode Size (%)	Max Depth	nCuts	KS-score for Signal (Background)
BP1	120	3	2.0	50	0.013 (0.078)
BP2	120	3	2.0	50	0.508 (0.41)
BP3	120	3	2.0	55	0.346 (0.041)
BP4	120	4	2.0	40	0.065 (0.028)

TABLE IX. The signal and background yields obtained using the BDTD analysis at 1 TeV ILC with 1000 fb^{-1} integrated luminosity corresponding to the signal BPs for the $e^+e^- \to 2\tau_h + \not{E}_T$ channel.

Benchmark point	Signal yield at 1000 fb^{-1}	Background yield at 1000 fb^{-1}	$\mathcal{L}_{5\sigma}$ (fb^{-1})
BP1	339	30	22
BP2	215	14	30
BP3	22	3	375
BP4	10	9	2979

TABLE X. Benchmark points used for studying the discovery prospects of an A in the muon-specific $(2+1)$HDM. The values for the rest of the masses are $M_H = M_{H^+} = 150$ GeV, $M_{\eta^+} = M_{\eta_R} + 1$ GeV $= 100$ GeV.

	SP1	SP2
m_{12}	22.8 GeV	21.6 GeV
$\tan\beta$	42.94	47.98
M_A	153.28 GeV	228.74 GeV
M_{η_I}	292.0 GeV	569.5 GeV
k_1	−1.74673	−2.27451
ω_1	1.3069	−3.12903
σ_1	−4.20973	−5.4915
σ_2	4.32283	6.06956
σ_3	6.14496	−5.5669
Δa_μ	1.47372	1.38208
BR$(\eta_I \to \eta_R A)$	0.971753	0.633975
BR$(A \to \mu^+\mu^-)$	0.998527	0.999054

TABLE XI. Signal and background cross sections for muon-specific $(2+1)$HDM at the 1 TeV ILC.

Signal/Backgrounds	Process	Cross section (fb) for P3
Signal		
SP1	$e^+e^- \to \eta_R\eta_I \to \eta_R\eta_R A \to \mu^+\mu^- + \not{E}_T$	9.74
SP2		2.42
Background	$e^+e^- \to 2\ell + \not{E}_T$	89.34

$\tau_{h_1}\tau_{h_2}$ cannot pinpoint M_A on account of the missing energy component of the τ decays. The $\not{E}_T$ spectrum of the signal BPs [Fig. 10(a)] in the muon-specific case also differs from the lepton-specific case. In the former, the only source of missing transverse energy is the DM particle η_R. And this implies a harder $\not{E}_T$ spectrum compared to the lepton-specific scenario wherein $\not{E}_T$ also draws a contribution from the neutrinos coming from τ decay. Given the $\mu^+\mu^-$ pair comes directly from the pseudoscalar, it gets tagged far more efficiently as opposed to what it would be with the involvement of an intermediate $\tau_\ell\tau_\ell$ pair. In all, $M_{\mu_1\mu_2}$ and $\not{E}_T$ are important observables to distinguish the signal from backgrounds for the muon-specific $(2+1)$HDM. In addition, the efficient identification of the muon momenta implies that the spectra of $p_T^{\mu_1\mu_2}$ and $p_{T_{\mu_1\mu_2}}^{\mathrm{vect}}$ for the signal BPs is also appreciably different from the $\not{E}_T$ background, as shown in Figs. 10(c) and 10(d).

We use the following kinematic variables for the BDTD analysis:

$$M_{\mu_1\mu_2},\quad p_T^{\mu_1},\quad p_T^{\mu_1\mu_2},\quad p_{T_{\mu_1\mu_2}}^{\mathrm{vect}},\quad \Delta R_{\mu_1\mu_2},\quad \not{E}_T,\quad \eta_{\mu_1},\quad \Delta\phi_{\mu_1,\not{E}_T},\quad \eta_{\mu_2},\quad \Delta\phi_{\mu_2,\not{E}_T},\quad \phi_{\mu_2},\quad \Delta\eta_{\mu_1\mu_2}. \tag{14}$$

The tuned BDTD parameters along with the KS scores for signal and background are given in Table XII. Once again, the definition of the variables should be clear from the notation. We have shown the ROC curve and the variation of significance with respect to BDT cut values

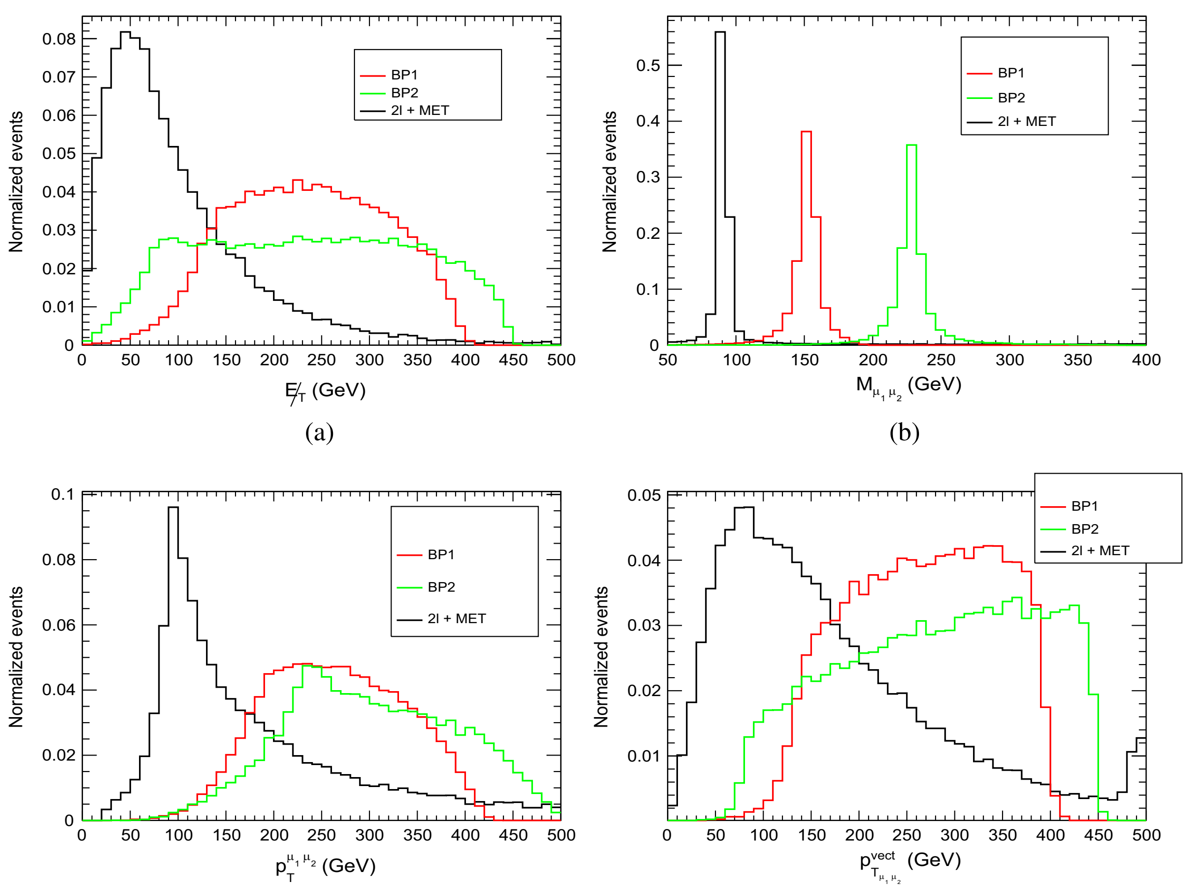

FIG. 10. The normalized distributions of $\not{E}_T, M_{\mu_1\mu_2}, p_T^{\mu_1\mu_2}, p_{T_{\mu_1\mu_2}}^{\mathrm{vect}}$ for $2\mu + \not{E}_T$ channel at 1 TeV.

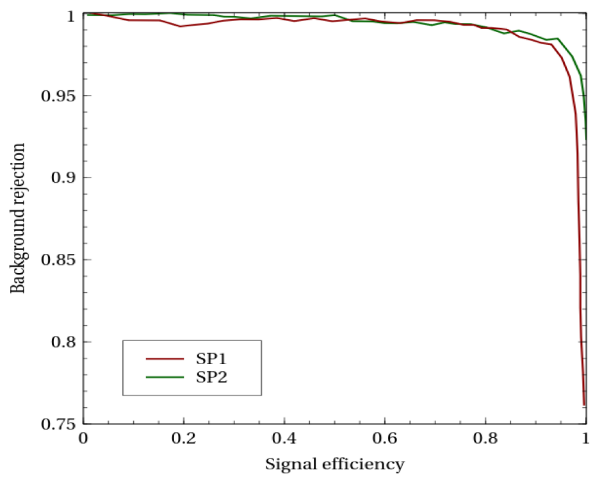

(a)

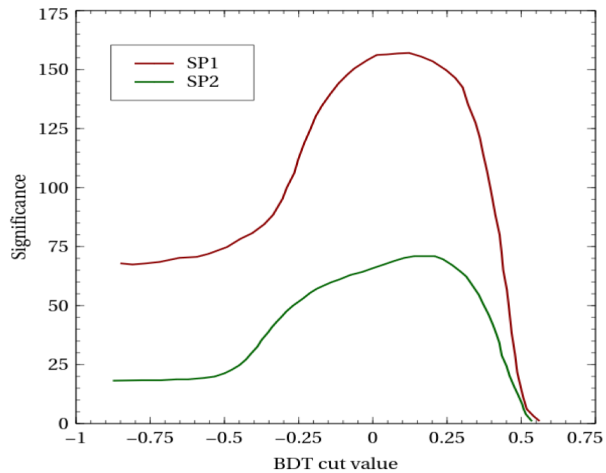

(b)

FIG. 11. (a) ROC curves for chosen benchmark points for $\mu^+\mu^- + \not{E}_T$ channel. (b) BDT scores corresponding to SP1, SP2 for $\mu^+\mu^- + \not{E}_T$ channel.

TABLE XII. Tuned BDT parameters for SP1, SP2 for the $2\mu + \not{E}_T$ channel.

	NTrees	MinNodeSize (%)	MaxDepth	nCuts	KS-score for Signal (Background)
SP1	110	4	2.0	55	0.401 (0.872)
SP2	110	4	2.0	55	0.9 (0.162)

TABLE XIII. The signal and background yields at 1 TeV ILC with 1000 fb^{-1} integrated luminosity for SP1,SP2 for the $e^+e^- \to \mu^+\mu^- + \not{E}_T$ channel after performing the BDTD analysis.

Benchmark point	Signal yield at 1000 fb^{-1}	Background yield at 1000 fb^{-1}	$\mathcal{L}_{5\sigma}$ (fb^{-1})
SP1	7485	147	< 1
SP2	1834	115	$\sim$4

in Figs. 11(a) and 11(b), respectively. After carrying out the BDTD analysis, the signal and the background yields at an integrated luminosity 1000 fb^{-1} along with the required luminosity for obtaining 5σ significance are given in Table XIII. The crucial points of differences between the lepton- and muon-specific analyses imply that the latter should offer a much higher observability than the former. An inspection of Table XIII reveals that an $M_A \simeq 230$ GeV in SP2 would require a mere 4 fb^{-1} integrated luminosity to get discovered.

V. SUMMARY AND CONCLUSIONS

We reprise the $(2+1)$HDM framework, that is, a 2HDM augmented with an additional scalar doublet. The scenario is endowed with a $\mathbb{Z}_2$ symmetry under which the additional doublet is negatively charged. Thus, the neutral CP-even component of the same is rendered cosmologically stable and becomes a potential DM candidate. The contribution to the muon anomalous magnetic moment from the $(2+1)$HDM has been examined in detail in the previous studies. And it was shown that a muon $g-2$ in the observed ballpark is obtainable in the $(2+1)$HDM for a much heavier pseudoscalar A than what it would be in the 2HDM. In this work, we look for signatures of such a setup at an e^+e^- collider operating at $\sqrt{s} = 1$ TeV with polarized beams. In addition to the canonical lepton-specific Yukawa interactions, we also consider a muon-specific variant in this study. We find that the signal cascades $e^+e^- \to \eta_R\eta_I \to \eta_R\eta_R A \to \tau^+\tau^- + \not{E}_T$ and $e^+e^- \to \eta_R\eta_I \to \eta_R\eta_R A \to \mu^+\mu^- + \not{E}_T$ are promising to probe the pseudoscalar A in the lepton- and muon-specific cases, respectively.

We have put forth benchmark points that are carefully filtered after applying the relevant constraints. Such constraints include the theoretical restrictions of perturbative unitarity and stability conditions as well as the experimental limits from Higgs signal strengths, oblique parameters and dark matter direct detection. It is ensured that $M_{\eta_I} > M_{\eta_R} + M_A$ for all the benchmarks such that the decay mode $\eta_I \to \eta_R A$ is kinematically open. We have further chosen the polarization configuration $(P_{e^-}, P_{e^+} = 80\%R, 30\%L)$ in the study since it predicts the maximum signal-to-background ratio. Multivariate analyses are subsequently carried out using the BDTD algorithm to improve the signal significance.

We analyze all three possible decay possibilities of the $\tau^+\tau^-$ pair, fully leptonic, semileptonic and fully hadronic. The semileptonic and fully hadronic modes predict overwhelmingly better observabilities than the fully leptonic mode. This is expected given the much higher efficiency of tagging a hadronic τ than a leptonic one. While the semileptonic and the fully hadronic mode show competing results, the latter fares better in case of $M_A \simeq 400$ GeV (BP4), the heaviest pseudoscalar amongst all the benchmarks. For this case, a 5σ discovery is expected at 3000 fb^{-1} integrated luminosity. In contrast, a similar statistical significance in the case of the LHC is limited to $M_A < 250$ GeV in the LHC.

The $\mu^+\mu^- + \not{E}_T$ channel is cleaner final state offering the $\mu^+\mu^-$ invariant mass as a handle to look for the A directly. When such kinematics is combined with the sizeable production $\mu^+\mu^- + \not{E}_T$ cross sections for the muon-specific signal benchmarks, this channel turns out to be generously promising. We have shown that M_A up to $\simeq$230 GeV can be discovered at 5σ for an integrated luminosity as low as 4 fb^{-1}. This further upholds the prospects of the e^+e^- machine to probe a leptophillic pseudoscalar.

ACKNOWLEDGMENTS

I. C. acknowledges financial support from Department of Science and Technology, Gov. of India, under Grant No. IFA18-PH214 (INSPIRE Faculty Award). N. C. acknowledges financial support from Department of Science and Technology, Gov. of India, under Grant No. IFA19-PH237 (INSPIRE Faculty Award).

APPENDIX: EXPRESSIONS OF VARIOUS CONTRIBUTIONS TO Δa_μ

The numerical expressions for the various Δa_μ contributions in the $(2+1)$HDM are given below. Here the loop order and the particle circulating in the loop are denoted by the superscript and the subscript, respectively. The one-loop contributions (shown in Fig. 12) at the alignment limit look like

$$\Delta a_{\mu(H)}^{(1\,\mathrm{loop})} = \frac{M_\mu^2}{8\pi^2 v^2}\left(\frac{M_\mu^2}{M_H^2}\right)(\xi_\mu^H)^2 \int_0^1 dx \frac{x^2(2-x)}{\left(\frac{M_\mu^2}{M_H^2}\right)x^2 - x + 1}, \tag{A1a}$$

$$\Delta a_{\mu(A)}^{(1\,\mathrm{loop})} = -\frac{M_\mu^2}{8\pi^2 v^2}\left(\frac{M_\mu^2}{M_A^2}\right)(\xi_\mu^A)^2 \int_0^1 dx \frac{x^3}{\left(\frac{M_\mu^2}{M_A^2}\right)x^2 - x + 1}, \tag{A1b}$$

$$\Delta a_{\mu(H^+)}^{(1\,\mathrm{loop})} = \frac{M_\mu^2}{8\pi^2 v^2}\left(\frac{M_\mu^2}{M_{H^+}^2}\right)(\xi_\mu^A)^2 \int_0^1 dx \frac{x^2(1-x)}{\left(\frac{M_\mu^2}{M_{H^+}^2}\right)x(1-x) - x}. \tag{A1c}$$

Numerical evaluation shows that $\Delta a_{\mu(H^+)}^{(1\,\mathrm{loop})} < 0$.

Next let us list out all the relevant two-loop Barr-Zee topologies contributing to Δa_μ. First we draw the Feynman diagrams featuring fermions in the one loop in Figs. 13(a) and 13(b).

Expressions for the corresponding two-loop amplitudes are

$$\Delta a_{\mu\{f,H\gamma\gamma\}}^{(2\,\mathrm{loop})} = \sum_f \frac{\alpha_{\mathrm{em}} M_\mu^2}{4\pi^3 v^2} N_C^f Q_f^2 \xi_f^H \xi_\mu^H \mathcal{F}^{(1)}\left(\frac{M_f^2}{M_H^2}\right), \tag{A2a}$$

$$\Delta a_{\mu\{f,A\gamma\gamma\}}^{(2\,\mathrm{loop})} = \sum_f \frac{\alpha_{\mathrm{em}} M_\mu^2}{4\pi^3 v^2} N_C^f Q_f^2 \xi_f^A \xi_\mu^A \tilde{F}^{(1)}\left(\frac{M_f^2}{M_A^2}\right), \tag{A2b}$$

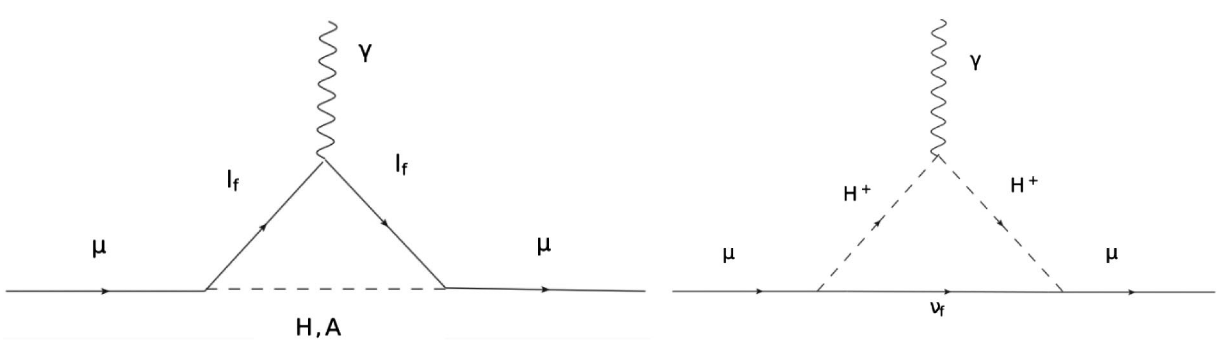

(a) (b)

FIG. 12. One-loop contributions to Δa_μ from (a) H, A and (b) H^+ in the loop.

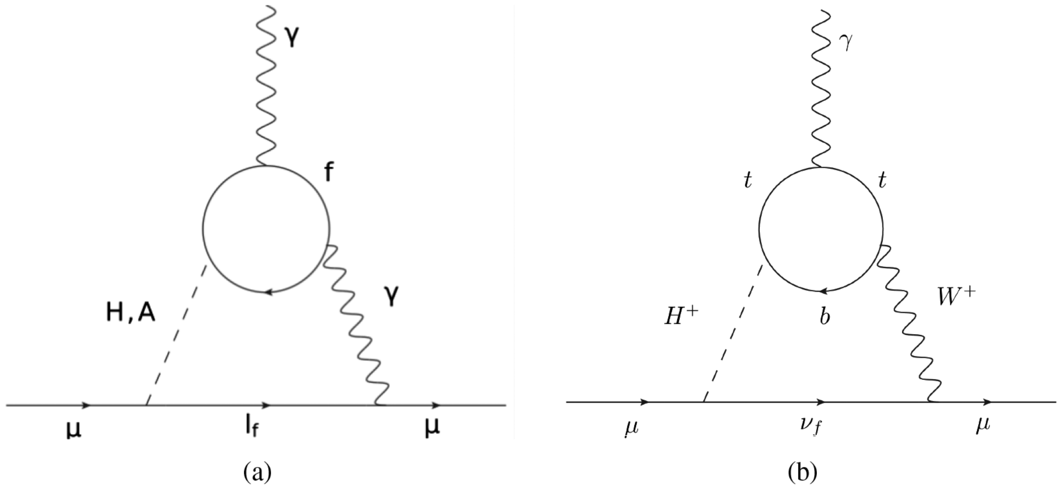

FIG. 13. Two-loop contributions to Δa_μ from the fermions through (a) an effective $\phi\gamma\gamma$ vertex with $\phi = H, A$ and (b) an effective $H^+W^-\gamma$ vertex.

$$\Delta a_{\mu\{f,H^+W^-\gamma\}}^{(2\,\mathrm{loop})} = \frac{\alpha_{\mathrm{em}} M_\mu^2 N_t |V_{tb}|^2}{32\pi^3 s_w^2 v^2 (M_{H^+}^2 - M_W^2)} \int_0^1 dx [Q_t x + Q_b(1-x)] \times [\xi_d^A \xi_\mu^A M_b^2 x(1-x) + \xi_u^A \xi_\mu^A M_t^2 x(1+x)] \times \left[\mathcal{G}\left(\frac{M_t^2}{M_{H^+}^2}, \frac{M_b^2}{M_{H^+}^2}, x\right) - \mathcal{G}\left(\frac{M_t^2}{M_W^2}, \frac{M_b^2}{M_W^2}, x\right)\right]. \quad \text{(A2c)}$$

Here, $N_C^f = 1(3)$ for leptons (quarks). Further, α_{em} denotes the fine structure constant and $Q_t = 2/3$, $Q_b = -1/3$. Next we come to the two-loop amplitudes with 2HDM scalars in the loops as shown in Figs. 14(a), 14(b) and corresponding amplitudes become

$$\Delta a_{\mu\{H^+,S\gamma\gamma\}}^{(2\,\mathrm{loop})} = \sum_{S=h,H} \frac{\alpha_{\mathrm{em}} M_\mu^2}{8\pi^3 M_S^2} \xi_\mu^S \lambda_{SH^+H^-} \mathcal{F}^{(2)}\left(\frac{M_{H^+}^2}{M_S^2}\right), \quad \text{(A3a)}$$

$$\Delta a_{\mu\{S,H^+W^-\gamma\}}^{(2\,\mathrm{loop})} = \frac{\alpha_{\mathrm{em}} M_\mu^2}{64\pi^3 s_w^2 (M_{H^+}^2 - M_W^2)} \sum_{S=h,H} \xi_\mu^S \lambda_{SH^+H^-} \int_0^1 dx x^2(x-1) \times \left[\mathcal{G}\left(1, \frac{M_S^2}{M_{H^+}^2}, x\right) - \mathcal{G}\left(\frac{M_{H^+}^2}{M_W^2}, \frac{M_S^2}{M_W^2}, x\right)\right]. \quad \text{(A3b)}$$

Finally, we depict the contributions from the inert scalars in loop in Figs. 15(a) and 15(b), with corresponding contributions:

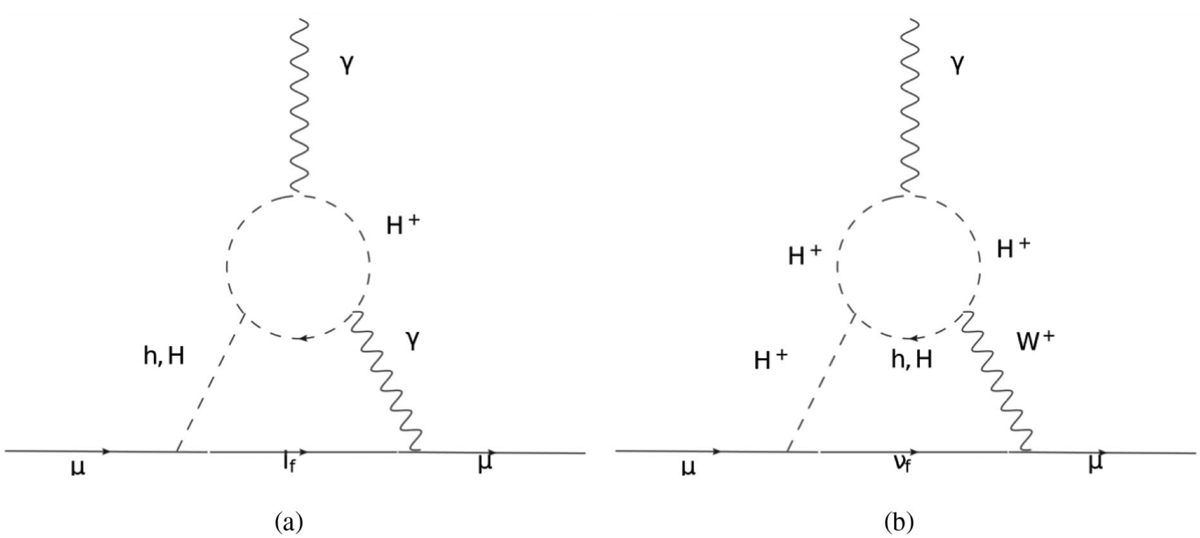

FIG. 14. Two-loop contributions to Δa_μ from the 2HDM scalars through (a) an effective $S\gamma\gamma$ vertex with $S = h, H$ and (b) an effective $H^+W^-\gamma$ vertex.

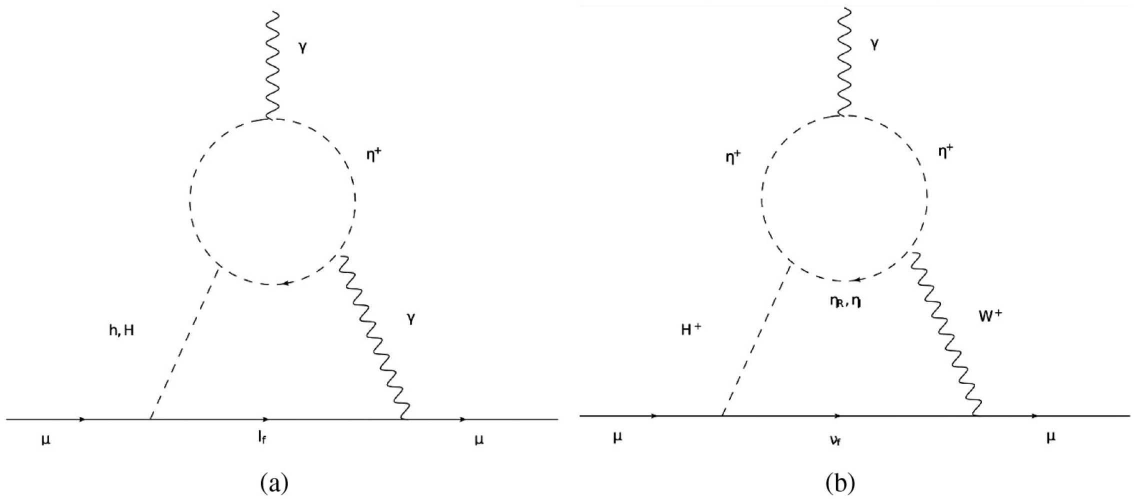

FIG. 15. Two-loop contributions to Δa_μ from the inert scalars through (a) an effective $S\gamma\gamma$ vertex with $S = h$, H and (b) an effective $H^+W^-\gamma$ vertex.

$$\Delta a_{\mu\{\eta^+, S\gamma\gamma\}}^{(2\,\mathrm{loop})} = \sum_{S=h,H} \frac{\alpha_{\mathrm{em}} M_\mu^2}{8\pi^3 M_\phi^2} \xi_\mu^S \lambda_{S\eta^+\eta^-} \mathcal{F}^{(2)}\left(\frac{M_{\eta^+}^2}{M_S^2}\right), \tag{A4a}$$

$$\Delta a_{\mu\{\eta, H^+W^-\gamma\}}^{(2\,\mathrm{loop})} = \frac{\alpha_{\mathrm{em}} M_\mu^2}{64\pi^3 s_w^2 (M_{H^+}^2 - M_W^2)} \xi_\mu^A \lambda_{H^+\eta^-\eta_R} \int_0^1 dx x^2 (x-1) \times \left[\mathcal{G}\left(\frac{M_{\eta^+}^2}{M_{H^+}^2}, \frac{M_{\eta_R}^2}{M_{H^+}^2}, x\right) - \mathcal{G}\left(\frac{M_{\eta^+}^2}{M_W^2}, \frac{M_{\eta_R}^2}{M_W^2}, x\right)\right] \tag{A4b}$$

$$+ \frac{\alpha_{\mathrm{em}} M_\mu^2}{64\pi^3 s_w^2 (M_{H^+}^2 - M_W^2)} \xi_\mu^A \lambda_{H^+\eta^-\eta_I} \int_0^1 dx x^2 (x-1) \times \left[\mathcal{G}\left(\frac{M_{\eta^+}^2}{M_{H^+}^2}, \frac{M_{\eta_I}^2}{M_{H^+}^2}, x\right) - \mathcal{G}\left(\frac{M_{\eta^+}^2}{M_W^2}, \frac{M_{\eta_I}^2}{M_W^2}, x\right)\right]. \tag{A4c}$$

The functions $\mathcal{F}^{(1)}(z), \tilde{\mathcal{F}}^{(1)}(z), \mathcal{F}^{(2)}(z)$, and $\mathcal{G}(z^a, z^b, x)$ can be defined as

$$\mathcal{F}^{(1)}(z) = \frac{z}{2} \int_0^1 dx \frac{2x(1-x) - 1}{z - x(1-x)} \ln\left(\frac{z}{x(1-x)}\right), \tag{A5a}$$

$$\tilde{\mathcal{F}}^{(1)}(z) = \frac{z}{2} \int_0^1 dx \frac{1}{z - x(1-x)} \ln\left(\frac{z}{x(1-x)}\right), \tag{A5b}$$

$$\mathcal{F}^{(2)}(z) = \frac{1}{2} \int_0^1 dx \frac{x(1-x)}{z - x(1-x)} \ln\left(\frac{z}{x(1-x)}\right), \tag{A5c}$$

$$\mathcal{G}(z^a, z^b, x) = \frac{\ln\left(\frac{z^a x + z^b(1-x)}{x(1-x)}\right)}{x(1-x) - z^a x - z^b(1-x)}. \tag{A5d}$$

[1] M. E. Peskin and D. V. Schroeder, *An Introduction to Quantum Field Theory* (Addison-Wesley, Reading, MA, 1995).

[2] T. Blum, A. Denig, I. Logashenko, E. de Rafael, B. L. Roberts, T. Teubner *et al.*, The muon (g-2) theory value: Present and future, arXiv:1311.2198.

[3] T. Blum, P. A. Boyle, V. Gülpers, T. Izubuchi, L. Jin, C. Jung, A. Jüttner, C. Lehner, A. Portelli, and J. T. Tsang (RBC and UKQCD Collaborations), Calculation of the Hadronic Vacuum Polarization Contribution to the Muon Anomalous Magnetic Moment, Phys. Rev. Lett. **121**, 022003 (2018).

[4] A. Keshavarzi, D. Nomura, and T. Teubner, Muon $g-2$ and $\alpha(M_Z^2)$: A new data-based analysis, Phys. Rev. D **97**, 114025 (2018).

[5] M. Davier, A. Hoecker, B. Malaescu, and Z. Zhang, A new evaluation of the hadronic vacuum polarisation contributions to the muon anomalous magnetic moment and to $\alpha(m_Z^2)$, Eur. Phys. J. C **80**, 241 (2020).

[6] T. Aoyama *et al.*, The anomalous magnetic moment of the muon in the Standard Model, Phys. Rep. **887**, 1 (2020).

[7] G. Colangelo, M. Hoferichter, and P. Stoffer, Two-pion contribution to hadronic vacuum polarization, J. High Energy Phys. 02 (2019) 006.

[8] M. Hoferichter, B.-L. Hoid, and B. Kubis, Three-pion contribution to hadronic vacuum polarization, J. High Energy Phys. 08 (2019) 137.

[9] K. Melnikov and A. Vainshtein, Hadronic light-by-light scattering contribution to the muon anomalous magnetic moment revisited, Phys. Rev. D **70**, 113006 (2004).

[10] M. Hoferichter, B.-L. Hoid, B. Kubis, S. Leupold, and S. P. Schneider, Dispersion relation for hadronic light-by-light scattering: Pion pole, J. High Energy Phys. 10 (2018) 141.

[11] T. Blum, N. Christ, M. Hayakawa, T. Izubuchi, L. Jin, C. Jung, and C. Lehner, Hadronic Light-by-Light Scattering Contribution to the Muon Anomalous Magnetic Moment from Lattice QCD, Phys. Rev. Lett. **124**, 132002 (2020).

[12] P. A. Zyla *et al.* (Particle Data Group), Review of particle physics, Prog. Theor. Exp. Phys. **2020**, 083C01 (2020).

[13] G. W. Bennett *et al.* (Muon g-2 Collaboration), Final report of the muon E821 anomalous magnetic moment measurement at BNL, Phys. Rev. D **73**, 072003 (2006).

[14] B. Abi *et al.* (Muon $g-2$ Collaboration), Measurement of the Positive Muon Anomalous Magnetic Moment to 0.46 ppm, Phys. Rev. Lett. **126**, 141801 (2021).

[15] G. C. Branco, P. M. Ferreira, L. Lavoura, M. N. Rebelo, M. Sher, and J. P. Silva, Theory and phenomenology of two-Higgs-doublet models, Phys. Rep. **516**, 1 (2012).

[16] A. Broggio, E. J. Chun, M. Passera, K. M. Patel, and S. K. Vempati, Limiting two-Higgs-doublet models, J. High Energy Phys. 11 (2014) 058.

[17] J. Cao, P. Wan, L. Wu, and J. M. Yang, Lepton-specific two-Higgs doublet model: Experimental constraints and implication on Higgs phenomenology, Phys. Rev. D **80**, 071701 (2009).

[18] L. Wang and X.-F. Han, A light pseudoscalar of 2HDM confronted with muon g-2 and experimental constraints, J. High Energy Phys. 05 (2015) 039.

[19] T. Han, S. K. Kang, and J. Sayre, Muon $g-2$ in the aligned two Higgs doublet model, J. High Energy Phys. 02 (2016) 097.

[20] V. Ilisie, New Barr-Zee contributions to $(g-2)_\mu$ in two-Higgs-doublet models, J. High Energy Phys. 04 (2015) 077.

[21] T. Abe, R. Sato, and K. Yagyu, Lepton-specific two Higgs doublet model as a solution of muon $g-2$ anomaly, J. High Energy Phys. 07 (2015) 064.

[22] A. Crivellin, J. Heeck, and P. Stoffer, A Perturbed Lepton-Specific Two-Higgs-Doublet Model Facing Experimental Hints for Physics Beyond the Standard Model, Phys. Rev. Lett. **116**, 081801 (2016).

[23] E. J. Chun and J. Kim, Leptonic precision test of leptophilic two-Higgs-doublet model, J. High Energy Phys. 07 (2016) 110.

[24] A. Cherchiglia, P. Kneschke, D. Stöckinger, and H. Stöckinger-Kim, The muon magnetic moment in the 2HDM: Complete two-loop result, J. High Energy Phys. 01 (2017) 007.

[25] X.-F. Han, T. Li, L. Wang, and Y. Zhang, Simple interpretations of lepton anomalies in the lepton-specific inert two-Higgs-doublet model, Phys. Rev. D **99**, 095034 (2019).

[26] E. J. Chun, J. Kim, and T. Mondal, Electron EDM and Muon anomalous magnetic moment in two-Higgs-doublet models, J. High Energy Phys. 12 (2019) 068.

[27] A. Dey, J. Lahiri, and B. Mukhopadhyaya, Muon $g-2$ and a type-X two Higgs doublet scenario: Some studies in high-scale validity, Phys. Rev. D **106**, 055023 (2022).

[28] D. Chowdhury and O. Eberhardt, Update of global two-Higgs-doublet model fits, J. High Energy Phys. 05 (2018) 161.

[29] L. Wang, J. M. Yang, M. Zhang, and Y. Zhang, Revisiting lepton-specific 2HDM in light of muon $g-2$ anomaly, Phys. Lett. B **788**, 519 (2019).

[30] E. J. Chun, S. Dwivedi, T. Mondal, and B. Mukhopadhyaya, Reconstructing a light pseudoscalar in the Type-X two Higgs doublet model, Phys. Lett. B **774**, 20 (2017).

[31] E. J. Chun, S. Dwivedi, T. Mondal, B. Mukhopadhyaya, and S. K. Rai, Reconstructing heavy Higgs boson masses in a type X two-Higgs-doublet model with a light pseudoscalar particle, Phys. Rev. D **98**, 075008 (2018).

[32] F. J. Botella, F. Cornet-Gomez, and M. Nebot, Electron and muon $g-2$ anomalies in general flavour conserving two Higgs doublets models, Phys. Rev. D **102**, 035023 (2020).

[33] F. J. Botella, F. Cornet-Gomez, C. Miró, and M. Nebot, Muon and electron $g-2$ anomalies in a flavor conserving 2HDM with an oblique view on the CDF M_W value, Eur. Phys. J. C **82**, 915 (2022).

[34] A. M. Sirunyan *et al.* (CMS Collaboration), Search for an exotic decay of the Higgs boson to a pair of light pseudoscalars in the final state of two muons and two τ leptons in proton-proton collisions at $\sqrt{s} = 13$ TeV, J. High Energy Phys. 11 (2018) 018.

[35] N. Chakrabarty, Muon $g-2$ in a type-X 2HDM assisted by inert scalars: A test at the LHC, preceding paper, Phys. Rev. D **107**, 075012 (2023).

[36] A. R. Johansen and M. Sher, Electron/muon specific two Higgs doublet model at e^+e^- colliders, Phys. Rev. D **91**, 054021 (2015).

[37] Y. Kajiyama, H. Okada, and K. Yagyu, Electron/muon specific two Higgs doublet model, Nucl. Phys. **B887**, 358 (2014).

[38] T. Abe, R. Sato, and K. Yagyu, Muon specific two-Higgs-doublet model, J. High Energy Phys. 07 (2017) 012.

[39] M. Raju, A. Mukherjee, and J. P. Saha, Investigation of $(g-2)_\mu$ anomaly in the μ-specific 2HDM with vector like leptons and the phenomenological implications, arXiv:2207.02825.

[40] P. A. Zyla, R. M. Barnett, J. Beringer, O. Dahl, D. A. Dwyer *et al.* (Particle Data Group), Review of particle physics, Prog. Theor. Exp. Phys. **2020**, 083C01 (2020).

[41] N. Aghanim *et al.* (Planck Collaboration), Planck 2018 results. VI. Cosmological parameters, Astron. Astrophys. **641**, A6 (2020).

[42] A. Semenov, LanHEP: A Package for the automatic generation of Feynman rules in field theory. Version 3.0, Comput. Phys. Commun. **180**, 431 (2009).

[43] G. Bélanger, F. Boudjema, A. Goudelis, A. Pukhov, and B. Zaldivar, micrOMEGAs5.0: Freeze-in, Comput. Phys. Commun. **231**, 173 (2018).

[44] E. Aprile *et al.* (XENON Collaboration), Dark Matter Search Results from a One Ton-Year Exposure of XENON1T, Phys. Rev. Lett. **121**, 111302 (2018).

[45] H. Abramowicz *et al.*, The international linear collider technical design report—Volume 4: Detectors, arXiv:1306.6329.

[46] A. Alloul, N. D. Christensen, C. Degrande, C. Duhr, and B. Fuks, FeynRules 2.0—A complete toolbox for tree-level phenomenology, Comput. Phys. Commun. **185**, 2250 (2014).
[47] J. Alwall, R. Frederix, S. Frixione, V. Hirschi, F. Maltoni, O. Mattelaer, H.-S. Shao, T. Stelzer, P. Torrielli, and M. Zaro, The automated computation of tree-level and next-to-leading order differential cross sections, and their matching to parton shower simulations, J. High Energy Phys. 07 (2014) 079.
[48] R. Frederix, S. Frixione, V. Hirschi, D. Pagani, H. S. Shao, and M. Zaro, The automation of next-to-leading order electroweak calculations, J. High Energy Phys. 07 (2018) 185.
[49] T. Sjöstrand, S. Ask, J. R. Christiansen, R. Corke, N. Desai, P. Ilten, S. Mrenna, S. Prestel, C. O. Rasmussen, and P. Z. Skands, An introduction to PYTHIA 8.2, Comput. Phys. Commun. **191**, 159 (2015).
[50] J. de Favereau, C. Delaere, P. Demin, A. Giammanco, V. Lemaître, A. Mertens, and M. Selvaggi (DELPHES 3 Collaboration), Delphes 3, A modular framework for fast simulation of a generic collider experiment, J. High Energy Phys. 02 (2014) 057.
[51] A. Hocker *et al.*, TMVA—Toolkit for multivariate data analysis, arXiv:physics/0703039.
[52] A. Adhikary, N. Chakrabarty, I. Chakraborty, and J. Lahiri, Probing the $H^{\pm}W^{\mp}Z$ interaction at the high energy upgrade of the LHC, Eur. Phys. J. C **81**, 554 (2021).
[53] W.-S. Hou, R. Jain, and C. Kao, Searching for extra Higgs bosons via $pp \to H, A \to \tau\mu, \tau\tau$ at the large hadron collider, arXiv:2202.04336.
[54] R. K. Ellis, I. Hinchliffe, M. Soldate, and J. J. van der Bij, Higgs decay to $\tau^+\tau^-$: A possible signature of intermediate mass Higgs bosons at the SSC, Nucl. Phys. **B297**, 221 (1988).